JOURNAL OF QUATERNARY SCIENCE (2022) **37**(7) 1189–1206 ISSN 0267-8179. DOI: 10.1002/jqs.3432

JQS Journal of Quaternary Science QRA Quaternary Research Association

How reliable is μXRF core scanning at detecting tephra layers in sedimentary records? A case study using the Lake Suigetsu archive (central Japan)

DANIELLE MCLEAN,[1,2]* PAUL G. ALBERT,[1] GORDON SCHLOLAUT,[3] HENRY F. LAMB,[4,5] MICHAEL H. MARSHALL,[4,6] ACHIM BRAUER,[7] JON WADE,[8] TAKESHI NAKAGAWA[9] and VICTORIA C. SMITH[2]

[1]Department of Geography, Swansea University, Swansea, UK
[2]Research Laboratory for Archaeology and the History of Art, University of Oxford, Oxford, UK
[3]German Research Centre for Geosciences (GFZ), Section: Climate Dynamics and Landscape Evolution, Telegrafenberg, Potsdam, Germany
[4]Department of Geography and Earth Sciences, Aberystwyth University, Aberystwyth, UK
[5]Botany Department, School of Natural Sciences, Trinity College Dublin, Ireland
[6]Institute of Education, University of Derby, Derby, UK
[7]Climate Dynamics and Landscape Evolution, GFZ German Centre for Geosciences, Potsdam, Germany
[8]Department Earth Sciences, University of Oxford, Oxford, UK
[9]Research Centre for Palaeoclimatology, Ritsumeikan University, Shiga, Japan

Received 14 January 2022; Revised 24 March 2022; Accepted 5 April 2022

ABSTRACT: Here, we evaluate the ability of micro X-ray fluorescence (μXRF) core scanning to identify non-visible volcanic ash (cryptotephra) layers in sedimentary records. Its suitability is assessed using the annually resolved lacustrine sediments of Lake Suigetsu (Japan) for which there is high-resolution ITRAX μXRF core scanning data, and a detailed crypto-tephrostratigraphy (formerly established via density separation techniques). The studied core sections contain 10 visible and 30 cryptotephra markers that span a range of glass concentrations (from 1000 to >20 000 shards per gram of dried sediment) and compositions (basalts, trachy-andesites, phonolites, trachytes and rhyolites), thus providing an ideal case study. The ITRAX core scanner produced recognisable μXRF elemental responses for the visible ash layers, including those just 1 mm thick. However, just 10% of the cryptotephra layers could be unequivocally identified. Although this study demonstrates that μXRF core scanning should not be used as an independent method within a similar geological setting, we show it can provide a powerful tool alongside traditional techniques. Where detected, μXRF profiles can verify and refine cryptotephra positions (here to a sub-millimetre resolution), and help establish reworking signatures. These insights create possibilities for ultra-precise synchronisation of records, improved chronological modelling and help generate more complete eruption histories.

KEYWORDS: Tephra Detection; ITRAX; Lake Suigetsu; Lake sediment; μXRF core scanning.

Introduction

Distal deposits of volcanic ash (tephra) preserved in sedimentary sequences (lacustrine, peat and marine) are excellent chronological markers for dating and correlating palaeoenvironmental and archaeological records (Davies *et al.*, 2012; Smith *et al.*, 2013; Blockley *et al.*, 2014; Lane *et al.*, 2014; Lowe *et al.*, 2015; Lane *et al.*, 2017) and thus are highly sought after within Quaternary studies. In addition, these layers provide an important resource for volcanologists investigating the frequency, eruptive magnitude and dispersal of past explosive events (e.g. Costa *et al.*, 2012; Schindlbeck *et al.*, 2018; Di Roberto *et al.*, 2018; Albert *et al.*, 2018, 2019; Buckland *et al.*, 2020; McLean *et al.*, 2020a). Such is the value of these markers, it is increasingly worthwhile to search for fine ash layers, which due to their low or diluted glass concentrations are only microscopically preserved (i.e. cryptotephra layers) in sedimentary profiles (Pyne-O'Donnell *et al.*, 2012; Barton *et al.*, 2015, 2021; Davies, 2015; Wulf *et al.*, 2018; Chen *et al.*, 2016, 2019; Timms *et al.*, 2019; McLean *et al.*, 2018; Panaretos *et al.*, 2021). Detailed cryptotephra investigations have meant that coeval isochrons can be identified over wide geographical regions (over thousands of kilometres; Lane *et al.*, 2011; Jensen *et al.*, 2014; Ponomareva *et al.*, 2015; McLean *et al.*, 2016; van der Bilt *et al.*, 2017; Cook *et al.*, 2018; Kearney *et al.*, 2018; Jones *et al.*, 2020), and permit the construction of more complete volcanic records, allowing the integration of lower magnitude events and/or eruptions from more distal sources (e.g. Albert *et al.*, 2018). Indeed, in some instances cryptotephra layers may prove to be the only geological evidence of some eruption events (McLean *et al.*, 2020b).

Conventional density separation methods for the identification and characterisation of cryptotephra layers are notoriously time-consuming (e.g. >30 h to process 1 m of sediment), highly iterative, and can require significant amounts of valuable core material. As a result, it is often not feasible to undertake detailed cryptotephra investigations over long stratigraphic intervals. Even for benchmark Quaternary palaeoclimate records, and those providing the most robust

*Correspondence: D. McLean, Department of Geography, as above.
E-mail: danielle.mclean@arch.ox.ac.uk

tephrostratigraphies, many sequences have only been assessed in part, or at low resolutions over certain time periods (e.g. the Greenland ice cores). The most reliable and widely utilised method to identify low-concentration ash layers in marine and lacustrine records is achieved by separating the volcanic glass grains from the host sediments. This is typically accomplished using density separation techniques that are able to extract the volcanic glass shards from the lighter (typically organic) and denser (minerogenic) components, and allow for the primary positioning of the cryptotephra peak (i.e. the eruption event) to be identified (see Turney, 1998; Hall and Pilcher, 2002; Turney *et al.*, 2004; Blockley *et al.*, 2005; Davies *et al.*, 2007). As such, this method requires a contiguous and destructive sampling strategy, multiple grade sieving, petrography and microscopy at a range of stratigraphic resolutions. A detailed approach is critical in interpreting low primary inputs of glass, since even moderate reworking and taphonomic biases can skew or obscure the shard distribution profile (see Davies, 2015). For instance, taphonomic processes caused by inflows to lakes have been shown to affect the preservation of cryptotephra layers (Pyne-O'Donnell, 2011), weathering of the local geology can cause secondary inwash events (MacLeod and Davies, 2016), and patchy tephra distribution can be caused by fallout on snow (Bergman *et al.*, 2004).

Although typically utilised to understand the nature of sediments and environmental responses to climatic change, micro X-ray florescence (μXRF) core scanning has been effectively used to identify and interpret thick, visible ash layers preserved in marine and lacustrine records (e.g. Dugmore and Newton, 1992; Vogel *et al.*, 2010; Damaschke *et al.*, 2013; McCanta *et al.*, 2015). It is possible to detect the positioning of these markers due to the contrast between the geochemical and mineralogical composition of the ash and the matrix/host sediments. μXRF core scanning is well suited to the analysis of long sedimentary cores, as the technique is non-destructive, can be operated at relatively high speed, high spatial resolutions (up to a 20 μm stepping interval on some systems) and requires almost no sample preparation (Croudace *et al.*, 2006; Thomson *et al.*, 2006; Croudace and Rothwell, 2010; Davies *et al.* 2015). An X-ray beam is used to analyse the split surface of the sediment core, and the geochemistry is determined using the unique wavelengths at which different elements fluoresce when excited (Francus *et al.*, 2009). It is therefore possible to generate a comprehensive time series of geological data and detect changes in particular single element profiles or profiles of element ratios. The composition of ash (glass and minerals with decipherable amounts of Si, K, Ca, Ti, Fe, Rb, Sr and Zr) are therefore likely to be reflected in the core scanning data and potentially show the precise position of high concentrations of ash and cryptotephra. Previous studies have shown that the elemental data generated for tephra layers using μXRF core scanning are not, however, comparable to individual shard analysis by electron microprobe (e.g. Kylander *et al.*, 2012; Peti *et al.*, 2020).

Significant questions still surround the ability of μXRF core scanning to detect both fine ash (i.e. <1 mm in thickness) and cryptotephra layers preserved in high-resolution sedimentary sequences, although the technique has been combined in a range of multiproxy studies to date (e.g. De Vleeschouwer *et al.*, 2008; Lim *et al.*, 2008; Vogel *et al.*, 2010; Wulf *et al.*, 2013; Zawalna-Geer *et al.*, 2016; Jouannic *et al.*, 2022). Earlier work has shown that, as for visible ash deposits, detection may largely depend on the contrast of the host sediment and the glass shards, in addition to the concentration of the grains (Moreno *et al.* 2007; Langdon *et al.* 2011; Kylander *et al.*, 2012; Cassidy *et al.*, 2014; McCanta *et al.*, 2015). As a result, its usefulness is thought to be more variable, depending on the archive and neighbouring volcanic region. Most commonly, useful elements for the detection of volcanic ash are typically K, Ca, Fe and Zr, with element ratios such as Ca/Ti and K/Ti being able to minimise the overprint of environmental signals also captured in the sediment. Experimental approaches have shown that the grain size can also play an important determinant in the detection of visible and cryptotephra layers when using μXRF core scanning. By spiking synthetic cores with rhyolitic and basaltic tephra layers in varying concentrations and glass particle sizes, Balascio *et al.* (2015) showed there was an inverse relationship between the grain size and the μXRF signal, likely caused by the tightness/compaction of the glass fragments. They also showed that the rhyolitic cryptotephra layers were difficult to detect, even at high glass concentrations. Similarly, Kylander *et al.* (2012) showed that it was possible to locate several high-concentration basaltic (>1000 shards/cm^3), but not low-concentration rhyolitic tephra layers (<859 shards/cm^3) based on a study using gyttja-rich sediment cores from the Faroe Islands. It is not yet clear whether there are specific thresholds of shard concentrations that are potentially required for detection, as well as the compositional impact of the host sedimentation. Particularly for Si-rich rhyolitic tephra layers, the concentration threshold is likely to be very high, perhaps even above those typically observed for cryptotephra, and exacerbated by the fact that quality Si data is difficult to obtain using μXRF core scanning systems (Kylander *et al.*, 2012). Moreover, Peti *et al.* (2020) showed that the μXRF profiles across fine ash and cryptotephra layers can be related to other analytical factors, including the position of the scanning track on the split core and surface drying.

Further studies are required, particularly in different geological and volcanic settings, to determine the percentage of (crypto)tephra layers that remain undetected when using μXRF core scanning as a first-order means of discrimination. Further work is required to quantify the success identification rate, potential thresholds for detection (i.e. glass compositions, grain size, concentrations) and provide an understanding of which elements and element ratios are useful for different volcanic centres/compositions. Moreover, it is also possible that μXRF core scanning could help to alleviate other longstanding problems faced by tephrochronologists when interpreting low concentrations of glass (e.g. discriminating primary/secondary peaks, identifying their precise positioning, and evaluating sediments with high background concentrations of volcanic glass). The applications of μXRF core scanning of cryptotephra alongside traditional methods are currently untested. If verified, this technique would have significant potential for the identification of sampling targets (i.e. sediments most likely to contain cryptotephra layers), speed up the processing time of searching for specific cryptotephra layers, and also increase the application of cryptotephra investigations.

This study uses the high-resolution and precisely dated sediments of Lake Suigetsu (Honshu Island, central Japan; Fig. 1) to evaluate the application of μXRF core scanning for detailed cryptotephra studies. We discuss several potential factors determining the discrimination of cryptotephra layers and outline further considerations for tephrochronologists utilising core scanning to generate complete eruptive records. The Lake Suigetsu lacustrine record has numerous characteristics that make it a suitable case study for this investigation.

1. Detailed visible and cryptotephra investigations (using conventional density separation techniques) have located 30 cryptotephra layers preserved in the Holocene (<10 ka; McLean *et al.*, 2018) and Marine Isotope Stage (MIS) 3

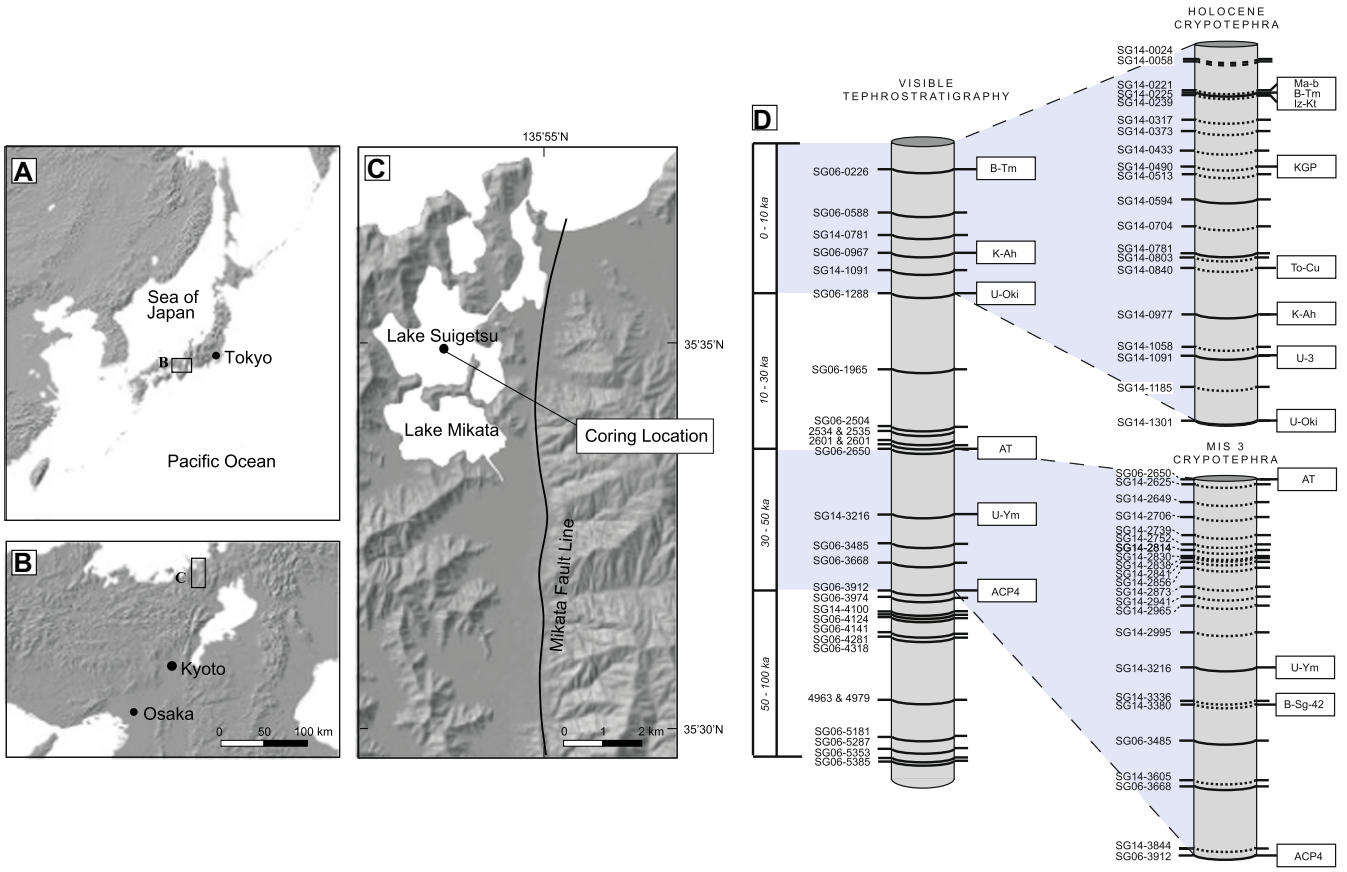

Figure 1. (a–c) Location of Lake Suigetsu, one of the Mikata Five Lakes, located in Fukui Prefecture, central Japan (modified after Nakagawa *et al.*, 2012). (d) Summary of the Lake Suigetsu SG06 tephrostratigraphy and positioning of the visible (solid line; Smith *et al.*, 2011, 2013; McLean *et al.*, 2016; Albert *et al.*, 2018, 2019) and non-visible (cryptotephra) layers (dashed line; McLean *et al.*, 2018, 2020a, b). Correlations to key widespread markers distributed across east Asia are shown in the white boxes and further stratigraphic information is provided in Table 1. The tephra layers vary in their glass concentrations (from *ca.* 1000 to >20 000 shards per gram) and originate from at least 16 different volcanic centres across east Asia. [Color figure can be viewed at wileyonlinelibrary.com]

sediments (50 to 30 ka; McLean *et al.*, 2020b) of Lake Suigetsu. These 40 tephra originate from 16 different volcanic centres across east Asia (e.g. Japan, South Korea, North Korea, China) and therefore incorporate a range of glass compositions and concentrations suitable for assessment.

2. Ultra-high μXRF elemental data (60 μm step-width, 100 μm vertical beam-width; see Section *High-resolution μXRF elemental scanning*) have been obtained from the Lake Suigetsu sediments (from the core top to 45 m composite depth (CD); Marshall *et al.*, 2012; Schlolaut *et al.*, 2012) providing detailed quantitative profiling across all identified cryptotephra and visible tephra layers.
3. A comprehensive analysis of event layers (e.g. those recording evidence of past flood and earthquake events) has been performed using thin-section microscopy and the μXRF elemental data (Schlolaut *et al.*, 2012, 2014, 2018). This work can be utilised and applied to investigate the characteristics of high-energy events that are known to have remobilised volcanic glass shards in the catchment and could skew cryptotephra assessments.
4. Thin sections of the sediments were previously prepared for microanalytical and varve analysis (Schlolaut *et al.*, 2014) and can be used here to further investigate the stratigraphic positioning of cryptotephra within the varved sediments.

This study is the first to investigate high-resolution μXRF elemental responses (e.g. 60 μm) across a long stratigraphic sequence (>30 m with varved and non-varved sediments), and for an abundance of glass shard concentrations and compositions (i.e. 40 tephra layers erupted from at least 16 different volcanic centres across east Asia).

Study site and sediments

Lake Suigetsu, catchment and coring campaigns

Lake Suigetsu (35°35′N 135°53′E, 0 m above sea level) is a small tectonic basin located close to the Sea of Japan, and situated in Fukui Prefecture (Fig. 1). The lake is 34 m deep and covers an area of 4.3 km^2 with a diameter of *ca.* 2 km. It is part of a tectonic lake system (the Mikata Five Lakes) with a small catchment area, vegetated by warm mixed forest and is surrounded by a ring of Palaeozoic hills (maximum elevation 400 m) (Nakagawa *et al.*, 2005). The main tributary feeding freshwater to the five Mikata lakes is the River Hasu (*ca.* 10 km in length), which enters on the southeastern side of Lake Mikata and flows through the Seto Channel into Lake Suigetsu. This channel is particularly shallow (*ca.* 2 m in depth), meaning that during high-energy hydrological events (such as floods), Lake Suigetsu receives only a small proportion of detrital material from the Hasu River catchment (Nakagawa *et al.*, 2012).

The geology around the lake is dominated by a large granite pluton to the east and southeast. To the south mudstone dominates, but sandstone, chert, limestone, basalt and dolerite also occur. There is sandstone at the northeast coast of the lake, while at the north and west coasts basalt, dolerite and chert are dominant (Schlolaut *et al.*, 2014). Schlolaut *et al.*

(2014) analysed 23 catchment samples (e.g. soil, rock, stream and rivulet sediments) from around the lake and the proximal watershed of the Hasu River. XRF analyses showed a strong anticorrelation between Ti and K. K is enriched in samples that are influenced by the granite pluton to the east, while the highest Ti values are found in the distal watershed of the Hasu River in the south and at the northeast coast of the lake (Fig. 8 of Schlolaut *et al.*, 2014). In general, the rocks are high in elements that are also present and characteristic of the regional silicic tephra fall (see Section *Lake Suigetsu tephrostratigraphy*, below), such as Si, K, Fe and Ca.

In this study we use sediment from the 'SG06' (cores A, B, C and D) and 'SG14' (E, F, G and H) coring campaigns, which were obtained near the depo-centre of Lake Suigetsu (see Nakagawa *et al.* 2012; Fig. 1). A composite stratigraphy was generated using marker layers identifiable in the parallel cores (e.g. tephras, turbidites and flood layers that are >4 mm thick) for both SG06 and SG14, which allowed for the substitution of any disturbed sediments. Here, we use the composite correlation model version 24 August 2009 which is age-modelled onto the IntCal13 timescale (Reimer *et al.*, 2013). The chronology is composed of 808 individual ^{14}C determinants, providing an integral component of the International ^{14}C Calibration (IntCal) dataset (Bronk Ramsey *et al.*, 2012; Reimer *et al.*, 2013, 2020; Staff *et al.*, 2011, 2013). The entire Suigetsu composite stratigraphy is estimated to cover the last 200 ka, with clear varve formation between 10 and 70 ka (Staff *et al.*, 2013).

Sediment characteristics and μXRF analyses

The sediments of Lake Suigetsu have been studied for over three decades following the first 4 m piston cores extracted in 1991 (Kitagawa and Van der Plicht, 1998a, b). For the majority of its sedimentation the lake basin was extremely stable, with anoxic conditions preventing bioturbation. The Suigetsu sediments consist of organic material, diatoms, siderite and detrital mineral grains, which form both the dominant matrix and distinct seasonal layers (Schlolaut *et al.*, 2012). The different seasonal inputs into the lake form compositionally different layers, which provide a baseline that varies quite significantly for most elements. In the varved sediments (i.e. 70–10 ka), a single year can produce multiple distinct seasonal layers which accumulate to a total annual thickness of between 0.2 and 1.25 mm, as revealed by thin-section analysis (Schlolaut *et al.*, 2014, 2018). While there are some variations due to different environmental settings over time, siderite, organic and detrital seasonal layers usually build the varve structure. In general, the sequence is composed of very fine sediments, since even during catastrophic events, the coarse-sized particles were preferentially deposited in Lake Mikata to the south (Fig. 1) before reaching Lake Suigetsu.

The first detailed μXRF study of Suigetsu sediments was published by Katsuta *et al.* (2007) using a Scanning X-Ray Analytical Microscope (SXAM), which used the 'SG04' core (obtained in 1993; Kitagawa *et al.*, 1995). Between 19.0 and 5.6 ka, they identified 33 event-related sedimentary layers including three tephra, silty clay and turbidite layers. Turbidites were characterised by periods of high Mn and Fe, and silty clay layers (interpreted as flood layers) by high Al, Si, K, Ca and Ti. Katsuta *et al.* (2007) suggested that the visible tephra layers did not coincide with peaks in Ti, unlike the other event-related layers.

High-resolution μXRF (using an ITRAX core scanner), thin-section microscopy and core photographs were used to undertake detailed sediment analysis and varve counts from the SG06 core top to 4497.7 cm CD (Marshall *et al.*, 2012; Schlolaut *et al.*, 2012, 2014, 2018). Microfacies analysis showed that the vast majority of the detrital layers preserved in the sediments were produced by flood events (362 of the 369) (Schlolaut *et al.*, 2014). Flood events could be distinguished from other major depositional events, such as landslides or subaqueous slope failures. In particular, the clastic event layers could be characterised in the SG06 profile using elements Ti, K, Ca and Si fluctuations. Indeed, Ti is a well-established tracer for terrigeneous input in lacustrine sequences (Yarincik and Murray, 2000). Peaks in K concentrations often indicate the presence of clays and/or K-feldspar, and Ca likely derives from detrital carbonates or plagioclase. The Si signature of the event layers is not as distinct as that of the other elements since the sediment is rich in diatoms and hence generally rich in Si. In general, Fe and Mn are also considered as two elements that show changes in the hydrology and sedimentation of the lake (Katsuta *et al.*, 2007; Marshall *et al.*, 2012). From the top down to 3095.9 cm SG06 CD the sediments are usually dominated by autochthonous components, while below (>38 213 cal. yrs BP) they contain a higher proportion of detrital mineral grains. This is evident in the μXRF signals that show a significant drop in Ti and Ca in the upper core sections, as well as a weak drop in K (Schlolaut *et al.*, 2014). It is proposed that the change from a clastic-rich to a clastic-poor facies may be related to change in the inflow point for the Hasu River, potentially shifting the estuary from Lake Suga to Lake Mikaka and 'turning the filter on' (Schlolaut *et al.*, 2014).

Lake Suigetsu tephrostratigraphy

The Lake Suigetsu tephrostratigraphy provides the single most comprehensive record of east Asian volcanism established to date. Thirty-two visible ash layers have been identified in the SG06 core (Smith *et al.*, 2011, 2013; McLean *et al.*, 2016; Albert *et al.*, 2018, 2019; Fig. 1), most of which originate from eruptions at calc-alkaline to high-K calc-alkaline arc volcanoes situated southwest of Suigetsu and were dispersed via the prevailing westerly winds. The thickest tephra beds preserved in the Lake Suigetsu sediments are therefore correlated to well-known caldera-forming eruptions (VEI 6–7) of four active or buried volcanoes situated on Kyushu Island (Kikai, Aira, Aso and Ata; see Smith *et al.*, 2013; Albert *et al.*, 2019). Many of the thinnest visible ash layers preserved in the SG06 core possess overlapping yet heterogeneous rhyolitic glass chemistries, and are correlated using their distinctive trace element signature to activity at two of the closest volcanoes, Daisen and Sambe, situated on the southwestern Japan Arc (Albert *et al.*, 2018). Other ash layers originate from alkali-rich intraplate volcanoes Ulleungdo (South Korea) and Changbaishan (North Korea/China border), which have also been very productive throughout the Late Quaternary (McLean *et al.*, 2020a). In general, most of the tephra layers vary in their relative abundances of major, minor and trace elements as shown by the electron microprobe and LA-ICP-MS analyses of the glass shards, although layers from Ulleungdo (U-2, U-3, U-4 and U-Ym) are largely geochemically indistinguishable (McLean *et al.*, 2020a).

Detailed cryptotephra analysis through the Lake Suigetsu sediments has significantly extended the tephrostratigraphy, from 32 to 62 layers and allowed for the integration of tephra isochrons from volcanic sources further afield (Fig. 1; McLean *et al.*, 2018, 2020b). In general, this work revealed four times as many cryptotephra layers relative to the visible layers that were preserved, providing an unprecedented record of eruptions that dispersed ash to the populated regions of central Honshu. Moreover, this work has helped generate more complete eruptive records; for instance, where only one visible ash layer was identified from Aso caldera, this has been supplemented by eight additional cryptotephra layers within the sediments dating between 50 and 30 ka (McLean *et al.*, 2020b). In the investigated sediments, at least one significant cryptotephra

Table 1. Overview of the investigated Lake Suigetsu sediments, the (crypto-)tephrostratigraphy and any ITRAX detection of tephra. Visible ash layers are shaded grey, and the cryptotephra layers that can be positively identified using compositional variations detected using a μXRF core scanner are shaded in green. Changes (above or below the baseline for the sediments) are typically observed in one of the following: Ca/Ti, K and/or Fe

Tephra Label	SG06 Composite Sampling Depth	Tephra (name, volcano)	Glass Shard Morphology	Glass Shard Concentration (s/g)	Visible Thickness (cm)	Glass composition		ITRAX detection of tephra?	Elements for detection in Suigetsu sediments		Single elements for detection	Useful element ratios	Position of μXRF Peak	Identification and Geochemical Reference
						K Series Classification	TAS Classification		Increase	Decrease				
SG14-0058	70.6 - 71.4	-	PU, MV, MI		-	-	-	No clear signal	Potential peak Mn	None	-	-		1
SG14-0221	220.5 - 221.6	Ma-b, Mashu	C, F, V, MV	1,675	-	Low	Rhyolite	No clear signal	Subtle peak at Ca/Ti	None	-	-		1
SG06-0226	**225.5**	**B-Tm, Changbaishan**	**C, V**	**Visible**	**0.1**	**High**	**Rhyolite**	**Yes**	**Fe, Ba, Ca/Ti, Sr/Ti**	**None**	**P, Fe, Pb**			2
SG14-0239	239.1 - 240.1	Iz-Kt, Kozushima	C	22,700	-	Medium	Rhyolite	No	None	None	Al, K, Ca, Ti, Fe, Zn, Rb (minor)			1
SG14-0433	429.0 - 430.0	U-1? Ulleungdo	PL, C	1,100	-	High	Trachyte	No	None	None	-	-		1
SG14-0490	484.0 - 485.0	KGP, Kawagodaira	C, F, V	>8,000	-	Medium	Rhyolite	Yes	K, Ca, Ti, Sr,	None	Si, K, Ca, Ti, Fe, Zn, Rb Sr	Ca/Ti, Sr/Ca, Ca/Rb	484.2	1
SG06-0588	**587.8**	**Th-pd, Sambe**	**PU, MI**	**>20,000**	**0.2**	**Medium**	Rhyolite	**Yes**	**K, Ca, Sr**	**None**	Si, K, Ca, Ti, Fe, Zn, Rb, Sr, Zr, Pb			1, 3, 4
SG14-0704	699.1 - 700.0	Kikai	PU, MV, MI	>8,000	-	Medium	Rhyolite	No	None	None	-	-		1
SG14-0781	**775.4**	**S2-fl, Sambe**	**PU, MI**	**Visible**	**0.1**	**Medium**	**Rhyolite**	**Yes**	**K, Ca, Sr,**	**None**	**Si, K, Ca, Zn, Sr, Zr, Ba**			1, 3, 4
SG14-0803	797.9 - 798.9	U2, Ulleungdo	MV	>20,000	-	High	Rhyolite	No	None	None	-	-		1
SG14-0840	835.9 - 836.9	To-Cu, Towada	C, MV	18,750	-	Low	Rhyolite	Yes, if use 1 cm average	Ca/Ti	None		Ca/Ti	836.3	1
SG06-0967	**967.2**	**K-Ah, Kikai**	**PL**	**Visible**	**2.8**	**Medium**	**Rhyolite**	**Yes**	**S, K, Ca, Ti, Sr, Zr,**	**Mn, Fe**	**K, Ca, Ti, Fe, Zn, Ga, Rb, Sr, Zr, Ba**			3
SG14-1058	1050.8 - 1051.8	B-SG-08, Changbaishan	C, F, V	21,383	-	High	Rhyolite	No clear signal	Potential Ba peak	None	-	-		1, 5
SG14-1091	**1085.2**	**U-3, Ulleungdo**	**MV**	**Visible**	**0.1**	**High**	**Phonolite/Trachyte**	**Yes, if use 1 cm average**	**Cl**	**None**	-	**K/Ti, Zr/Ti**		1, 5
SG14-1185	1180.2 - 1181.2	Unknown	MV, MI	9,786	-	Low	Rhyolite	No	None	None	-	-		1
SG06-1288	**1287.9**	**U-4, Ulleungdo**	**MV**	**Visible**	**1.9**	**High**	**Phonolitic/Trachytic**	**Yes**	**K, Ca, Rb, Sr, Zr, Ca/Ti, Sr/Ti**	**None**	**Si, Cl, K, Ca, Zn, Ga, Rb, Sr, Zr**			3, 6
SG14-2625	2655.6 - 2656.6	Aso	MI, C, V	9,838	-	High	Trachy-andesite/Andesite	No, obsured	Pb	None	S, Cl, Mn, Fe, Ni	-		7
SG14-2649	2676.1 - 2677.1	Aso	MI, PL	23,117	-	High	Rhyolite	No	None	None	-			7
SG14-2706	2729.9 - 2730.9	Ryukyu-Kyushu arc	F, V	>20,000	-	Medium	Rhyolite	No clear signal	Potential peak Ca/TI	None	-			7
SG14-2739	2762.2 - 2763.2	Aso	PL, MI	8,367	-	High	Trachyte	No clear signal	None	None	-			7
SG14-2752	2774.9 - 2775.9	Aso	F, C, MV	10,067	-	High	Trachyte/Rhyolite	No clear signal	None	None	-			7
SG14-2814	2835.3 - 2836.3	Aira	F	7,125	-	Medium	Rhyolite	No	None	None	-	-		7
SG14-2830	2851.1 - 2852.1	Ryukyu-Kyushu arc	PL	2,767	-	Medium	Rhyolite	No	None	None	-			7
SG14-2838	2858.9 - 2859.9	-	PU, MI	1,400	-	-	-	No	None	None	-			7
SG14-2841	2861.8 - 2862.8	Aso	PL, MI	2,850	-	High	Trachyte/Rhyolite	No	None	None	-			7
SG14-2856	2876.5 - 2877.5	Aira	C, V	1,482	-	Medium	Rhyolite	No	None	None	-	-	-	7
SG14-2873	2893.1 - 2894.1	Aira	F, V	12,575	-	Medium	Rhyolite	No	Potential Ba peak	None	-	-	-	7
SG14-2941	2956.8 - 2957.8	-	MI, P	>5,000	-	-	-	No	Potential Ca/Ti peak	None	-			7
SG14-2965	2980.5 - 2981.5	Kurile arc	V, MV, MI	1,950	-	Low	Rhyolite	No	None	None	-			7
SG14-2995	3008.5 - 3009.5	Ryukyu-Kyushu arc	V	>20,000	-	Medium	Rhyolite	No	None	None	-			7
SG14-3016	3029.1 - 3030.1	Ryukyu-Kyushu arc	PL, F	6,567	-	Medium	Rhyolite	No	None	None	-			7
SG14-3085	3094.9 - 3095.9	Aso	PU	4,400	-	High	Trachy-andesite	No, obsured signal	None	None	K, Ca, Ti, Mn, Fe, Zn, Rb ?	Mn/K	3095.1; 3096.2?	7
SG14-3216	**3223.7**	**U-Ym, Ulleungdo**	**MV**	**Visible**	**0.1**	**High**	**Phonolite/Trachyte**	**Yes**	**K, Zr, Ca/Ti**	**Ti, Fe**	**K, Ti, Fe, Zr**	**K/Ti, Zr/TI**		5, 7
SG14-3336	3352.1 - 3353.1	-	PU, MI	5,750	-	Medium	Rhyolite	Yes, but only using Sr	Sr	None	-	-		7
SG14-3380	3397.2 - 3398.2	B-SG-42, Changbaishan	MV, F	18,383	0.02	High	Trachytic	No clear signal	Ca/Ba	None	-	Ca/Ba	3396.3	5, 7
SG06-3485	**3485.3**	**Fuji**	**F, V, PL**	**Visible**	**0.5**	**Low**	**Basaltic-andesite**	**Yes**	**Ca, Sr, Ca/Ti**	**K, Ti, Fe**	**K, Ca, Ti, Fe, Cu, Zn, Rb, Sr**			3, 7, 8
SG14-3605	3628.7 - 3629.7	Aso	MI, G	2,200	-	High	Trachyte/Dacite	Yes, significant signal	Ca	K, Ti, Sr, Ba	K, Ca, Ti, Sr, Ba	Ca/Ti; Sr/Ti	33629.8	7
SG06-3668	**3667.8**	**SI, Sambe**	**PU, MV, F**	**>20,000**	**0.3**	**Medium**	**Rhyolite**	**Yes**	**Ca, Sr, Ca/Ti, Sr/Ti**	**Ti, Fe**	**K, Ca, Ti, Fe, Sr**			3, 4, 7
SG14-3844	3879.5 - 3880.5	Aira	F, V, MI	16,013	-	Medium	Rhyolite	No	None	None	-	-		7
SG06-3912	**3911.7**	**ACP4, Aso**	**F, C**	**Visible**	**0.1**	**High**	**Rhyolite**	**Yes**	**Minor peak in K, Ca, Ca/Ti**	**None**	**Ti**	**Ti/K or Ca/Ti**		3, 7, 8

References: 1) McLean *et al.* 2018; 2) McLean *et al.* 2016; 3) Smith *et al.* 2013; 4) Albert *et al.* 2018; 5) McLean et al. 2020a;6) Smith *et al.* 2011; 7) McLean*et al.* 2020b;8) Albert *et al.* 2019.
The correlation model used for the depth is version 24 August 2009. The exact master core positioning of the ash layers are published in the attached references.
PU = Pumiceous, PL = Platy, C = Cuspate, F = Fluted, V = Vesicular, MV = Microvesicular, MI = Microlite inclusions, G = Green.

layer is detected in each metre of sediment (an event approximately every 500 years), although there are periods that contain very high concentrations of background glass shards, reflecting reworking events, which are likely to mask other important cryptotephra layers (Fig. 1). Critically, detailed density separation work also identified numerous fine visible ash layers (~1 mm in thickness) that were not picked up by visual examinations of the cores, such as the B-Tm Changbaishan ash (McLean *et al.*, 2016). In summary, the tephra layers utilised in the time periods here vary in their glass concentrations (from 1000 to >20 000 shards per gram) and originate from at least 16 different volcanic centres across east Asia (reflected in their geochemical composition) (Table 1).

Materials and methods

Cryptotephra identification

As highlighted, high-resolution density separation techniques were employed throughout the 12 m of Holocene sediments (≤10 ka; McLean *et al.*, 2016, 2018) and more recently the 14 m of annually laminated (varved) sediments dating to between *ca.* 50 and 30 ka (McLean *et al.*, 2020a, b). The master SG14 core (composite sequence) was contiguously subsampled at a *ca.* 5 cm resolution avoiding the known high-energy event layers (e.g. flood horizons). If elevated shard concentrations were observed in the *ca.* 5 cm sample, the sediment was resampled at a 1 cm resolution to determine the precise stratigraphic positioning of the peak. The extracted glass shards were counted via microscopic examination to quantify the number of shards per gram of dried sediment (shards/gram). Glass shards were extracted from samples chosen for geochemical analysis and handpicked from a welled slide using a micromanipulator (see Lane *et al.*, 2014 for details). These shards were mounted in epoxy resin stubs, which were sectioned and polished to expose a flat surface, and carbon coated for electron microprobe analysis. Major and minor element compositions of individual glass shards were measured using a JEOL-8600 wavelength-dispersive electron microprobe at the Research Laboratory for Archaeology and History of Art, University of Oxford. These geochemical datasets can be found in the supplementary material of the references indicated in Table 1. Identified tephra layers in the Suigetsu sediments are named, and are referred to using their SG06 (correlation model 6 June 2017) or SG14 (correlation model 30 May 2016) core CD(s) in centimetres.

High-resolution μXRF elemental scanning

SG06 LL-channel core sections were scanned using the ITRAX core scanning facility at Aberystwyth University and was operated following the standard methodology outlined in Croudace *et al.* (2006). Rather than using a single spot X-ray beam, the ITRAX is equipped with a flat X-ray beam, measuring a rectangular window. In this way, grain-to-grain variances are averaged across the horizontal core axis, ensuring a stronger signal and predominance of the environmental signal through depth. This is particularly useful for the identification of cryptotephra layers, which may be patchy and/or of low concentration. For the analyses used here a 20 × 0.1 mm rectangular beam was used, with a step size of 60 μm, a count time of 4 s, a voltage of 30 kV, a current of 30 mA and a Mo X-ray tube. A more detailed description of the settings used is given by Marshall *et al.* (2012). To avoid spurious patterns and relationships between elements caused by the effects of organic matter and water content, all data are normalised to the incoherent plus coherent (inc + coh) scattering.

As an initial step, we utilise baselines across the μXRF core scanning data to determine typical variability in the host sediment composition across the Holocene and varved MIS 3 sediments. These baselines were adopted to help quantify significant peaks (i.e. elemental counts significantly above the known paleoenvironmental and varve signal), and provide an assessment of which tephra layers are distinctive when regarded in context (i.e. within periods of sedimentation spanning several metres). For instance, within the Holocene sediments (1290 to 20 cm SG06 CD) a baseline of 0.01 cps/(inc + coh scattering) for Ca is used (dotted red line marked on Fig. 2a), where 23 exceeding peaks are identified through the 11.7 m of sedimentation. For the varved sediments dated between 50 and 30 ka, a higher baseline of 0.02 cps for Ca was used until 3095.9 cm SG06 CD, and 0.15 cps from 3095.9 to 2650.0 cm SG06 CD (Fig. 2b). This accounts for the known sedimentological change, likely caused by the redirection of the River Hasu. Here, Ca and Sr were used as key denominator elements as they yielded strong intensities, and showed the highest contrast between the visible volcanic layers and background lacustrine sediments. Relative peaks in Mn, Fe, Ti, K and Ba were also used as possible proxies for ash, as these elements are found in high concentrations in the glass and minerals of volcanic material. Significant peaks in elemental counts (i.e. those above positive baselines) were compared with the known ash concentration (e.g. shards per gram of dried sediment as published in McLean *et al.*, 2018, 2020b) to determine whether these coincided with known, or potentially undetected, event layers (i.e. tephra or high-energy flood/earthquake events). In several instances, glass preserved in peaks that did not coincide with known cryptotephra layers were geochemically analysed as part of this study using the methodology outlined in McLean *et al.* (2018) to check for other compositionally unique ash horizons, but they were not found to be new cryptotephra layers.

As a second step, a 30 cm interval across the position of all tephra (10 visible and 30 cryptotephra layers) was assessed to utilise the high-resolution core scanning data (at both 60 μm and averaged 1 mm) and decipher potentially muted signals. This interval uses the same scanning parameters as listed above and is used to provide a more thorough investigation across all single, or ratios of elemental counts, and the opportunity to locate the precise stratigraphic positioning of the cryptotephra. The μXRF elemental responses for visible ash layers were used to help determine useful elements for cryptotephra identification, specifically those erupted from the same volcanic source and have similar glass compositions.

Thin section microscopy

In order to further investigate the stratigraphic preservation of cryptotephra layers within the Suigetsu varved sediments, we microscopically examined a thin section taken from core section B-17, known to contain the trachytic cryptotephra layer erupted from Changbaishan (SG14-3380; *ca.* 42 ka). Thin sections of the sediments were prepared previously for microanalytical and varve analysis at Lake Suigetsu (see Schlolaut *et al.*, 2014). Sediments from the LL-channels were cut into 10 cm long segments and freeze-dried and then impregnated with synthetic resin under vacuum. These blocks were then glued to glass slides and cut, ground and polished to produce a 20 μm thin slice suitable for microscopic analysis as shown here (Brauer and Casanova, 2001).

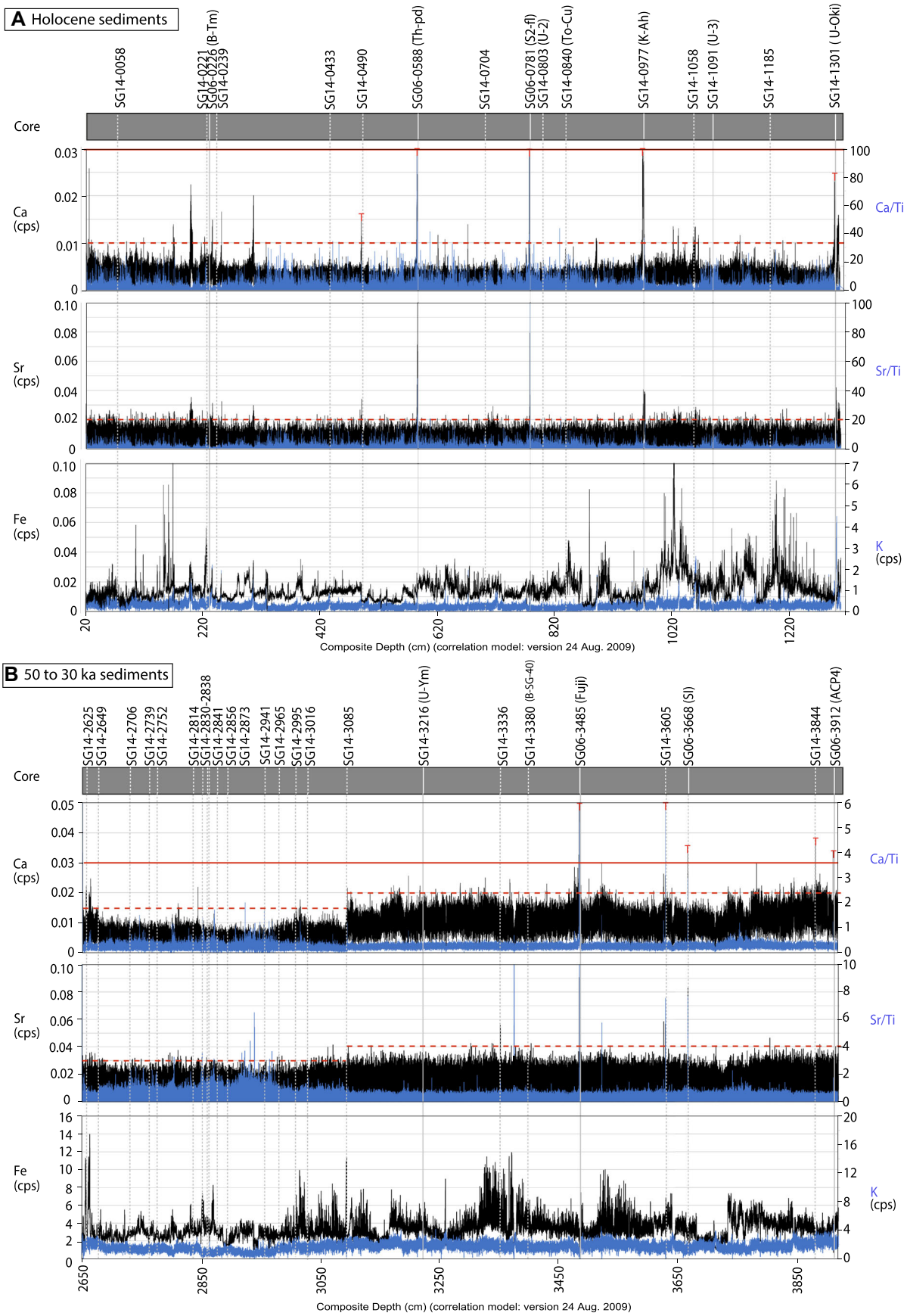

Figure 2. Overview of the ITRAX μXRF elemental compositions (in cps normalised to incoherent plus coherent) through the (a) Holocene and (b) MIS 3 Lake Suigetsu sediments. Significant peaks above these baselines (red dotted/bold horizontal lines) were compared with the ash concentrations (e.g. shards per gram of dried sediment) to determine whether these coincided with known or potentially undetected event layers (i.e. tephra or high-energy events). Tephra layers are delineated using a bold (visible) and dotted (cryptotephra) grey line, elemental responses of key tephra layers are capped with a red T. In order to only capture the geochemical enrichment caused by ash layers, the threshold for the Holocene and MIS 3 sediments needs to be >0.03 (cps) for Ca. [Color figure can be viewed at wileyonlinelibrary.com]

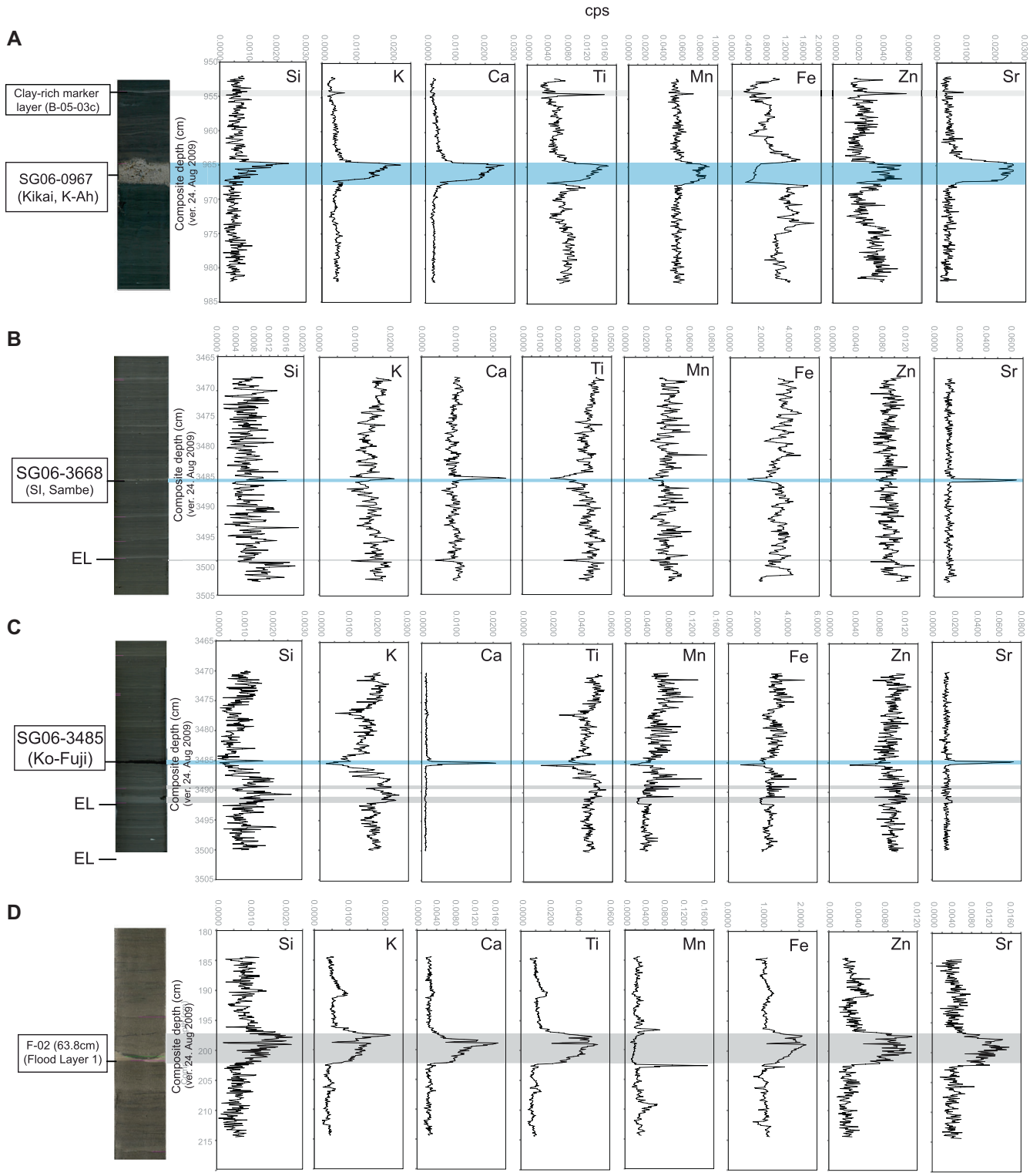

Figure 3. μXRF compositional variation (in cps normalised to incoherent plus coherent) across selected visible event layers (e.g. tephra and flood layers) in the Lake Suigetsu (SG06/SG14) sediments. The blue shading highlights the position of the visible tephra and the grey shaded boxes show the position of other high-energy event layers. [Color figure can be viewed at wileyonlinelibrary.com]

Results

Overview and baselines for tephra detection

Key elemental counts obtained by μXRF core scanning across the two sedimentary periods (i.e. the Holocene and MIS 3) are illustrated in Fig. 2. The studied sediments comprise different proportions of autochthonous (e.g. calcite precipitates, siderite, pyrite, diatoms) and allochthonous components (e.g. epiclastic, terrestrial plant remains, benthic diatoms) as reflected in the downcore data. For both periods, there is inherent variability throughout, as well as frequent and rapid deviation from baseline levels, particularly for Ti, Ca, K and Mn. As highlighted, the typical elemental counts of the host sediments change in MIS 3, with a relative drop in Ca, Ti and Sr stratigraphically above 3095.9 cm SG06 CD, followed by a greater sensitivity of Mn that frequently overprints the varve compositional baselines. In general, the μXRF core scanning counts throughout the Holocene are typically half those through the MIS 3 sediments. The most significant relative downcore compositional changes are positioned at visible

tephra (typically with relative enrichment in K, Ca, Sr and Ba; marked by a red 'T' on Fig. 2), reflecting the abundance of volcanic material, as well as other event layers caused by high-energy events such as floods/earthquakes (typically with relative increases in K, Ti, Fe).

In order to only capture the geochemical responses caused by ash layers, the threshold for the MIS 3 sediments needs to be >0.03 (cps) for Ca, which records five of the 30 ash layers (three visible and two cryptotephra; Fig. 2). A threshold of >2.0 (cps) for Ca/Ti incorporates three of these layers. For the Holocene sediments, count thresholds also need to be greater than >0.03 (cps) for Ca, which captures the position of four of the six visible ash layers, but none of the 30 cryptotephra layers. Lowering the baselines for these and other elements (e.g. Si, Al, Fe, K, Ti and Ba) in order to capture the peaks only attributed to tephra is not possible. For instance, a marginally lower Holocene baseline of 0.01 cps for Ca (red dashed line on Fig. 2a) incorporates 23 relative peaks, only one of which coincides with an additional cryptotephra layer (SG14-0490; KGP tephra).

In general, assessing the presence of ash layers in their broader stratigraphic context (i.e. across several metres of sedimentation) is challenging and requires a detailed understanding of the host sediment matrix and the possible palaeoclimatic influences through time. Detailed assessments using a more constrained stratigraphic interval (i.e. 30 cm), as well as utilising a range of single and/or ratios of two elements is often essential to identify elemental enrichment/depletion caused by the ash, and to rule out which peaks are attributed to other depositional processes. These specific elemental profiles are explored in more detail for all 10 visible and 30 cryptotephra layers in the following sections.

Elemental profiles across visible event layers

As highlighted, the most significant elemental peaks through the core occur at the position of visible ash (Figs 2 and 3) and delineate the position of seven of the 10 layers within the stratigraphic sequences of study (Table 1). Of these relative changes, the μXRF Ca/Ti profile across the basaltic–andesite tephra SG06-3485 (0.5 cm thick) is one of the most distinct, peaking at 10 times greater than the normal background/baseline variations at 5.5. This is to be expected as the glass shard compositions of this tephra are up to 10 times higher in CaO (8.5–10.6 wt.%) compared with the other layers in this study (Figs 2b and 3c). Its positioning also coincides with a relative decrease in K (Fig. 3c), not observed for other ash layers detected using μXRF core scanning, and must also relate to the glass compositions which contain 0.33–0.67 wt.% K_2O and are the lowest of the deposits investigated here. The three tephra layers erupted from Sambe volcano (central Japan) are also very clearly distinguishable within the host sediment compositions, with sharp enrichments in K, Ca, Ca/Ti, Sr and Sr/Ti, and relative depletions in Ti, Fe and Mn (Figs 2 and 3b; Table 1). These elemental responses clearly and precisely distinguish the tephra positions, despite their thicknesses being ≤0.3 cm.

Other fine ash visible layers (i.e. ranging in thickness between 0.1 and 0.2 cm) were not as easily identifiable in the μXRF core profiles, falling below the baseline Ca of 0.3 (cps), and also indicate the importance of glass compositions in their detection against the host sediment. These include the high-K (>4 wt.% K_2O) rhyolitic tephra layers erupted from Changbaishan and Aso ($n = 2$; 0.1 cm thick) and the phonolitic/trachytic tephra layers that erupted from Ulleungdo. Glasses erupted from Ulleungdo and Changbaishan show pronounced negative feldspar-related anomalies in Ba, Sr and Eu (McLean *et al.*, 2020a) and are abundant in major element contents that are already high in the host sediments and eroded rocks from the catchment (e.g. Al_2O_3, K_2O and CaO). Elemental peaks for these visible ash layers are therefore relatively subtle, but can be more easily recognised within a 30 cm stratigraphic interval, using Ti/K or Ca/Ti for Changbaishan, and K/Ti or Zr/Ti for Ulleungdo (Fig. 6; Table 1). The thin visible (0.1 cm) tephra that erupted from Aso (SG06-3912) contains glass with some of the highest K_2O content (4.46–4.90 wt.%) and also coincides with the largest K peak count. However, due to the significant downcore variability of this element, the SG06-3912 is not easily distinguished within a broader stratigraphic context (i.e. over several metres of sedimentation; Fig. 2b), and thus could easily be overlooked as a palaeoenvironmental or hydrological signal (Fig. 2).

A strong upcore signal/profile is observed within some of the thickest layers, this is most clearly demonstrated for SG06-0967 (K-Ah tephra), as shown in Fig. 3a. Since no chemo-stratigraphic variation occurs through this eruptive unit, it is interpreted that this strengthening must relate to the upwards fining (decreasing grain size, increased compaction) of the ash particles, which is also visible in the split cores. Interestingly, following the visible ash unit, the elemental spikes associated with the ash rapidly drops, even though the cryptotephra investigations show the sediment still contains very high concentrations of ash. For instance, baseline μXRF concentrations are reached almost immediately above the upper boundary of the K-Ah ash, whereas over 5000 shards per gram of sediment persist in the overlying 2 m (McLean *et al.*, 2018). A significant element response was observed for this rhyolitic tephra (e.g. enrichment in Si, K, Ca, Ti, Mn, Zn and Sr, and depletion in Fe; Fig. 2a) which replicates the 2.8 cm thickness of the visible deposit.

Other key fluctuations were observed in the μXRF data at the positions of known high-energy event layers defined previously in the core by Schlolaut *et al.* (2014). Several of these peaked over the baseline levels and concentrations observed associated with visible ash layers, for instance at 2923.4 cm SG06 CD (as marked on Fig. 2b), a position where no peak in glass shards was identified within the sediments. The visual characteristics and structure of the μXRF profiles for the significant high-energy events (see Schlolaut *et al.*, 2012) mean it is generally straightforward to discriminate between signals caused by ash or reworking deposits. Many event layers also coincide with significant increases in Ti, which is not typically observed for visible ash layers. However, the thick K-Ah ash unit is an exception to this, likely due to the considerable input of tephra and relatively high TiO_2 (*ca.* 0.54 wt.%) content of these rhyolitic glasses (Fig. 3a). Several of the thinner remobilisation events (i.e. <0.5 cm units that are visible in the core) are also newly identified by μXRF fluctuations, as highlighted on Figs 2 and 3.

Elemental profiles across positions of known cryptotephra layers

Overview

Just two of the 30 cryptotephra layers (SG14-0490 (Fig. 2a) and SG14-3605 (Fig. 2b)) could be clearly identified when plotting μXRF profiles for both study periods (e.g. Holocene or 50–30 ka; Fig. 2). These are recognised by significant elevations above baseline levels in K, Ca, Ti and Sr. When the known stratigraphic positioning of the cryptotephra layer is used, it is possible to detect muted responses for other layers

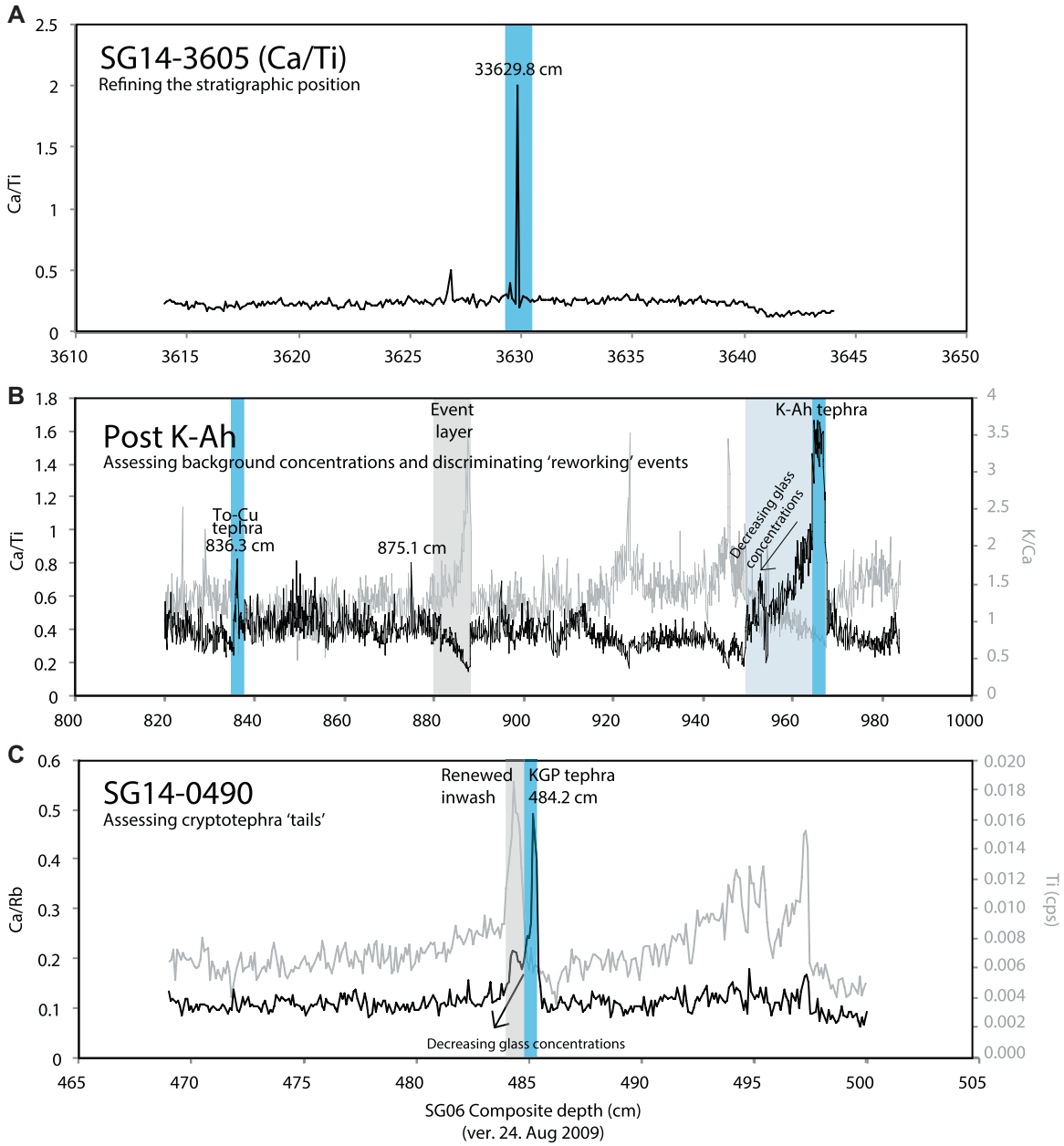

Figure 4. Selected μXRF elemental profiles over the positioning of several key visible and cryptotephra layers preserved in the Lake Suigetsu sediments. These examples highlight the ability of μXRF to assist in the identification and interpretation of the glass concentrations by: (a) refining the precision of the stratigraphic position of the peak; (b) the ability to identify primary cryptotephra layers during periods of high background glass concentrations (>5000 shard per gram), i.e. the To-Cu tephra at 836.3 cm CD (the compositional spike at 875.1 cm CD was investigated and it does not correspond to a tephra layer); and (c) the opportunity to track cryptotephra tails, renewed inwash events (using Ti) and determine the initial input/eruption position. The blue shading shows the position of the cryptotephra as determined by density separation techniques where the resolution is 1 cm. The grey bars show the position of crypto-event layers defined using the μXRF elemental responses shown. [Color figure can be viewed at wileyonlinelibrary.com]

across a defined 30 cm stratigraphic interval (SG14-0840; SG14-3316; SG14-3380; Table 1). Unlike that for the visible ash layers, there is no clear relationship with the elemental response and glass compositions. Furthermore, elemental baselines for detecting cryptotephra are not useful, as responses frequently fall below, or occur within, environmental transitions.

In cases where peaks in single or elemental ratio profiles are able to clearly delineate the cryptotephra marker, the stratigraphic position can be resolved at a greater level of precision, to between 0.1 and 0.2 cm, compared with the typical cryptotephra sampling resolution of 1 cm, which has been previously used for the Suigetsu sediments (McLean *et al.* 2018, 2020b; Table 1; Fig. 4a). This fine tuning of the ash layers' stratigraphic position is relevant for high-resolution correlation of records, which would better allow for spatial variations in proxy responses to climate to be identified. Furthermore, better stratigraphic resolution enables greater chronological age precision, and could potentially resolve eruptions to individual seasons.

Aso cryptotephra layers

During the varved MIS 3 sediments (i.e. 50–30 ka), three cryptotephra layers erupted from within the Aso caldera coincide with significant fluctuations observed in the μXRF profiles (Fig. 5). These cryptotephra layers include the andesitic/trachy-andesitic SG14-2625 (~61.8 wt.% SiO_2; 7.0 wt.% TAS), the andesitic SG14-3085 (dominant population ~57.3 wt.% SiO_2; 6.3 wt.% TAS) and the dacitic SG14-3605

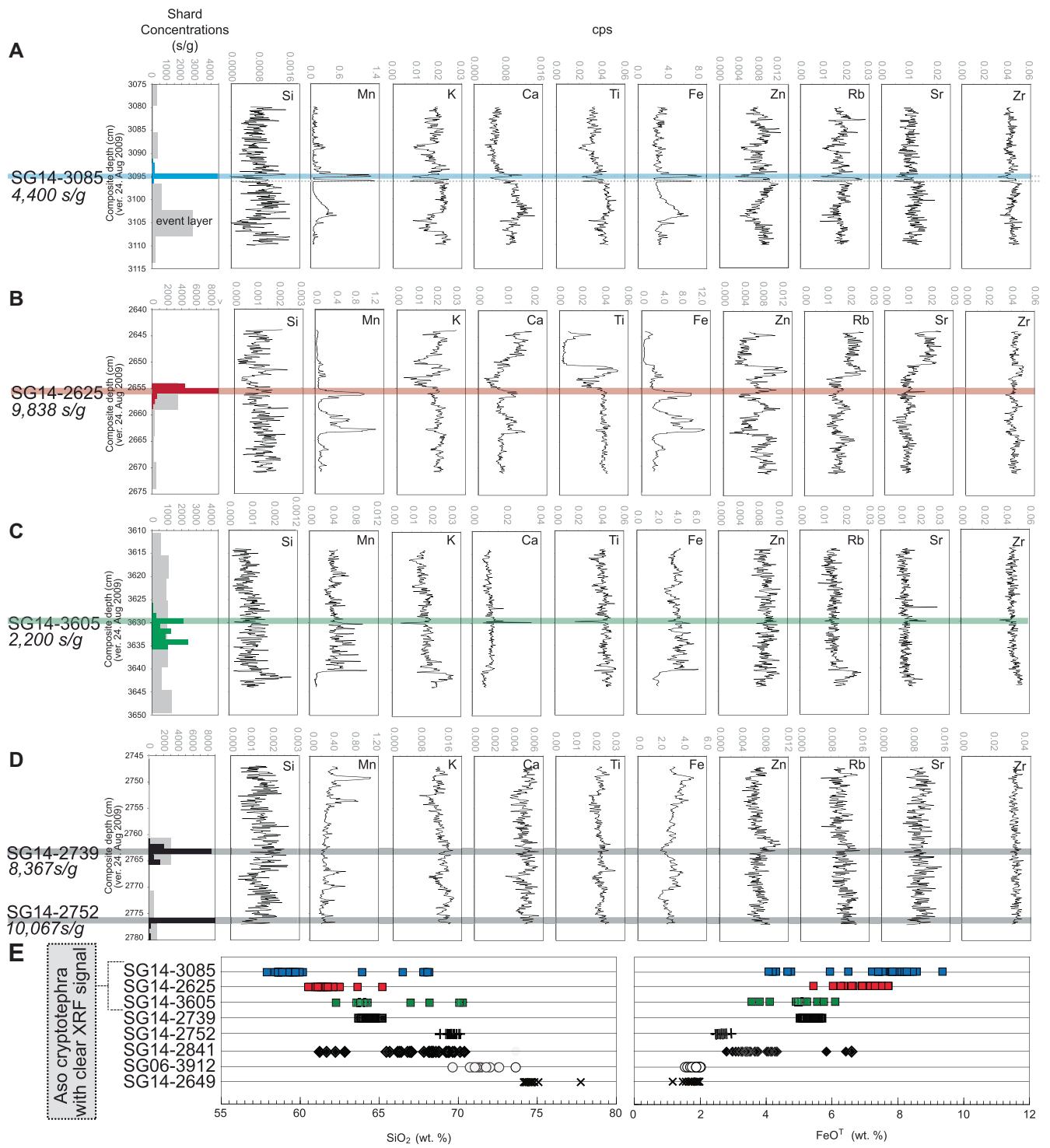

Figure 5. (a–d) Comparison of the glass shard concentrations (in shards per gram of dry sediment) and elemental profiles for Si, Mn, K, Ca, Ti, Fe, Zn, Rb, Sr and Zr (in cps normalised to incoherent plus coherent) across the known cryptotephra layers that have been correlated to eruptions of Aso (SG14-3085, SG14-2625, SG14-3605, SG14-2739 and SG14-2752). The cryptotephra counts are from McLean *et al.* (2020b). Horizontal lines indicate the positioning of the cryptotephra peak as determined using density separation techniques. (e) Glass compositions of the visible (e.g. SG06-3912) and cryptotephra layers erupted from Aso caldera and preserved in the Lake Suigetsu sediments between 50 and 30 ka (from McLean *et al.*, 2020b). [Color figure can be viewed at wileyonlinelibrary.com]

(~64.5 wt.% SiO_2; 7.8 wt.% TAS). The glass concentrations for these layers range from 2200 (SG14-3605) to 9838 shards per gram (SG14-2625; Fig. 5).

The most diagnostic μXRF elemental shifts for SG14-3085 and SG14-3605 are K, Ca, Ti, Cu, Zn, Rb and Ba, whereas S, Cl, Mn, Fe and Ni peaked at the position of SG14-2625 (Table 1). However, we interpret this as that SG14-2625 coincides with significant environmental/climatic response (represented by the dramatic changes in Mn and Fe), which masked any possible μXRF response to the ash deposit. This interpretation is strengthened by similar levels of fluctuations stratigraphically below where no peaks in ash are present (shown on Fig. 5b). The position of SG14-3605 (dacite; ~64.5 wt.% SiO_2; 7.8 wt.% TAS) is clearly determined using the μXRF core scanning data, even when assessing the values across the entire interval (e.g. 50–30 ka). Interestingly, this cryptotephra layer contains one of the lowest concentrations of glass shards (2200 shards per gram)

yet has a μXRF signal seemingly as strong as many of the visible ash layers (Fig. 2).

The core scanning elemental data show two significant peaks at the position of SG14-3085, which occur within 0.8 cm of sedimentation (Fig. 5a). This cryptotephra is positioned immediately following a thick event layer. This event layer was most likely deposited following a subaqueous slump, and is known to contain low concentrations of glass shards (Fig. 5a; McLean *et al.*, 2020b). The upper of the two μXRF peaks is defined by a significant increase in Ca and coincides with the position of the cryptotephra layer in the sediments. Further investigations using thin sections captured from these sediments revealed that both μXRF peaks coincide with fine-grained laminations, which may be caused by the formation of siderite or calcium carbonate. This sedimentological information gleaned using the thin sections highlight that other lake hydrological processes can cause very similar μXRF responses to the presence of glass shards.

The position of four other silicic tephra layers erupted from Aso (ranging from andesitic to rhyolitic in glass composition; Table 1) could not be identified using any single element profiles, or ratios including those that helped accentuate the rhyolitic visible Aso tephra (ACP4; Ti/K, Ca/Ti or Ca/Ba). These rhyolitic cryptotephra lack a clear μXRF response, despite glass concentrations exceeding 20 000 shards per gram in some cases.

Other rhyolitic cryptotephra layers

No significant μXRF responses were observed for the rhyolitic cryptotephra layers erupted from Aira caldera (SG14-2814, SG14-2856, SG14-2873 and SG14-3844), and others from undefined sources along the Ryukyu-Kyushu arc, all of which ranged in glass concentrations from 1550 shards per gram to over 16 000 shards per gram in the varved lake sediments. A single elemental spike in Sr is recognisable at the positioning of the rhyolitic cryptotephra SG14-3336, despite glass concentrations falling below 6000 shards per gram. Of the eight rhyolitic cryptotephra layers preserved in the non-varved Holocene sediments, only the high-K cryptotephra layer from Kawagodaira volcano (SG14-0490) with shard concentrations of >8000 shards per gram was clearly identifiable (Table 1; Fig. 4c). The most diagnostic single element and element ratio signals relate to Si, K, Ca, Ti, Fe, Zn, Rb, Pb, Ca/Ti and Sr/Ca. The μXRF profile suggests that the cryptotephra peak occurred at 485.2 cm CD, with a later inwashing event occurring at 484.4 cm CD with peaks in several other diagnostic elements including Ti (Fig. 4c). This is in close agreement with glass concentration counts (1 cm scan) which showed that the cryptotephra position fell between 484.0 and 485.0 cm SG06 CD (McLean *et al.*, 2018).

Ulleungdo and Changbaishan cryptotephra layers

Ratios of elements that were useful for the detection of the visible ash (U-3/SG14-1091; U-Oki/SG06-1288 and U-Ym/SG14-3216) deposits from Ulleungdo (i.e. K/Ti, Zr/Ti) were not able to detect a compositionally identical cryptotephra layer (SG14-0803), despite containing >20 000 shards per gram in the Suigetsu sediments (Fig. 6). A possible peak was observed for the U-2 tephra (SG014-0803) using Ca/Ba (Fig. 6d) but this is not particularly distinctive, and within the range of the sediments, and is not diagnostic. The trachytic cryptotephra erupted from Changbaishan (SG14-3380) can only be identified using Ca/Ba at 3396.3 cm SG06 CD, which is consistent with the low Ba concentrations in the SG14-3380 glass shards caused by K-feldspar fractionation.

Cryptotephra layers in high-background sediments

An elemental response (relative peak in Ca/Ti) for cryptotephra layer SG14-0840 (To-Cu) tephra was identified in the sediments following the thick K-Ah tephra (SG06-0967; Fig. 4b). These sediments contain very high concentrations of glass (18 750 shards per gram) that are predominantly derived from remobilisation or inwash of the K-Ah ash. The To-Cu eruption could be identified microscopically by a sharp change in the morphology of the glass shards (McLean *et al.*, 2018), which was confirmed by geochemical analysis. Other Ca/Ti peaks within this high background interval were investigated as part of this study to determine whether these positions also contained other primary ashfall deposits (i.e. at 875.1 cm CD). However, glass shard compositions from these positions were consistent with those for the K-Ah. Across this period other high-energy events and renewed inwash of the K-Ah tephra can be delineated using a K/Ca plot (Fig. 4b).

Refining the stratigraphic positioning of cryptotephra using μXRF core scanning

To further investigate the μXRF elemental responses across the cryptotephra layers, we examined a thin section taken from core section B-17, known to contain the trachytic cryptotephra layer erupted from Changbaishan (SG14-3380; *ca.* 42 ka). Density separation techniques showed that the cryptotephra marker contained 18 383 shards per gram and was therefore a likely candidate for identification in the μXRF core scanning data. Nonetheless, it was only possible to detect a compositional change in Ca/Ba across the 1 cm stratigraphic interval known to contain the Changbaishan glass (Fig. 6d).

Using the thin section, and the precise stratigraphic positioning determined by the Ca/Ba peak (i.e. 3396.3 cm SG06 CD), it was possible to microscopically locate the positioning of glass shards within the varved sediments (Fig. 7). The glass shards are situated along a small crack that was likely caused via freeze-drying when generating the thin section. As shown in Fig. 7, the shards are remarkably well constrained, forming a layer <200 μm thick within the sediments. These findings are significant, showing the excellent stratigraphic preservation of the glass shards in the varved sediments, which is not always the case for cryptotephra in other archives. Although this stratigraphic preservation is very useful for ultra-precise correlations between different records, as well as for precise chronological age modelling (perhaps here down to a seasonal resolution), this may not be ideal for detection via μXRF core scanning. The glass shards make up <20% of the total analysis, and without very distinctive glass compositions, a pronounced elemental signal is not likely.

Discussion

μXRF core scanning for the detection of cryptotephra layers

This investigation demonstrated that in this geological setting, the ITRAX core scanning data were not able to independently establish a detailed crypto-tephrostratigraphy. While distinct and recognisable elemental responses were evident for 7 out of ten visible tephra layers in the investigated time window, only 2 of the 30 cryptotephra layers were clearly resolved (Table 1; Fig. 2). Relative enrichments in K, Ca, Sr, Ca/Ti, Sr/Ti and sometimes Ca/Ba could be used to locate these ash layers, but there is no single element or ratio that can be used to unequivocally identify just the tephra layers. Due to the significant downcore variability of the sediment matrix,

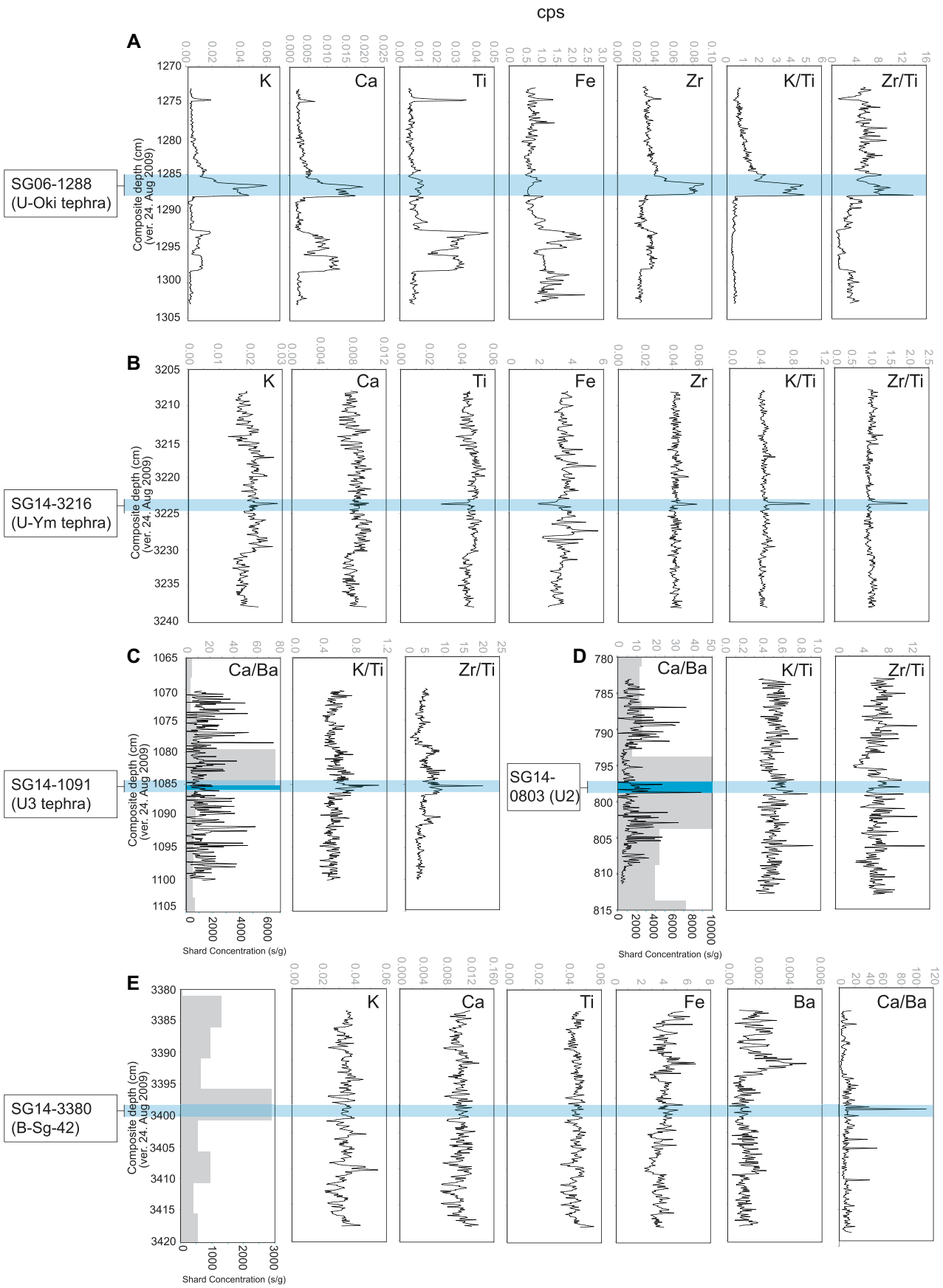

Figure 6. Comparison of the glass shard concentrations and elemental profiles across the positioning of known cryptotephra layers erupted from (a–d) Ulleungdo (SG06-1288, SG14-3216, SG14-1288 and SG14-1091) and (e) Changbaishan (SG14-3380). Horizontal blue lines indicate the positions of the cryptotephra peak as determined using density separation techniques (McLean *et al.*, 2020b). K/Ti and Zr/Ti elemental profiles were effective in identifying the position of the fine (1 mm thick) layers from Ulleungdo, but were not able to identify the high-concentration cryptotephra layer (U2 eruption). Ca/Ba was effective in positively locating the position of SG14-3380. [Color figure can be viewed at wileyonlinelibrary.com]

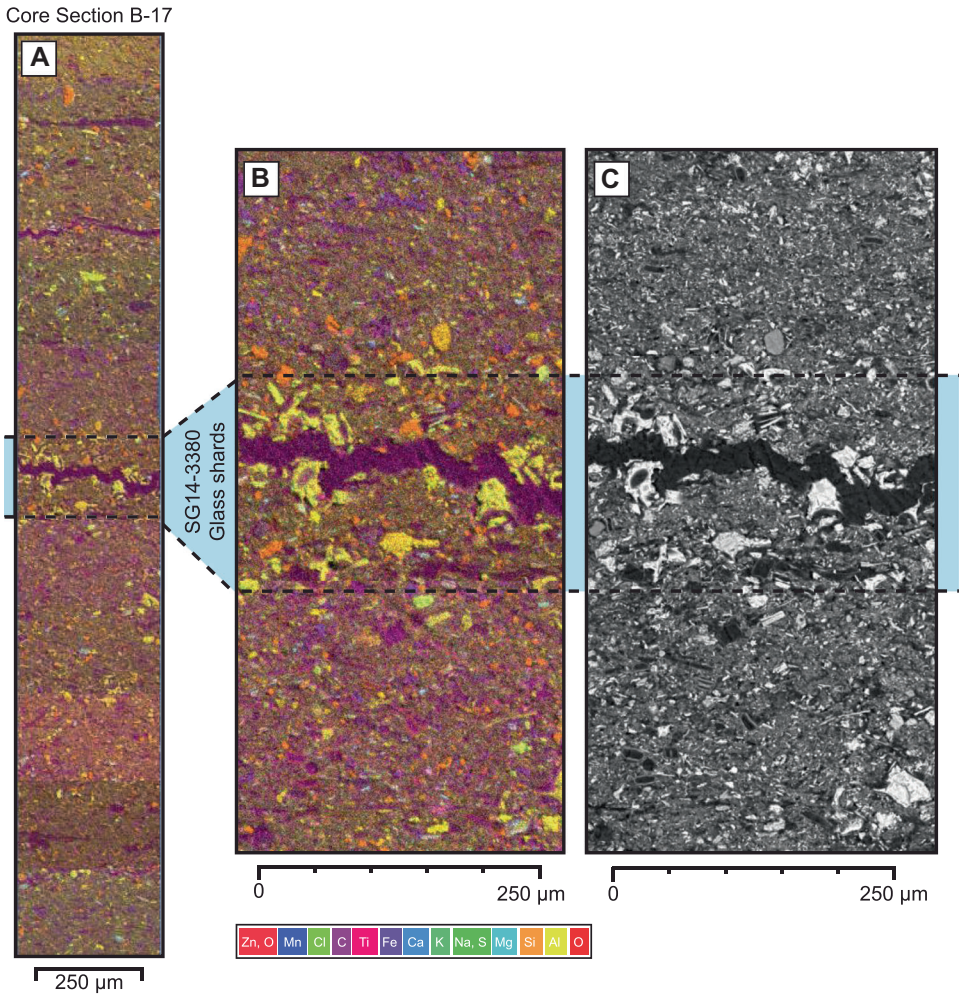

Figure 7. Thin section energy-dispersive X-ray spectroscopy (EDS) composition (a, b) and backscattered electron (BSE) (c) image showing the glass shards of SG14-3380 in core section B-17. This trachytic tephra that erupted from Changbaishan volcano (B-SG-42) is not visible in core sections but contains concentrations of 18 383 shards per gram (McLean *et al.*, 2020b). The glass shards are located in a small crack in the sediment and constrained to <200 µm in thickness. Even though numerous shards (tens to 50 µm in diameter) are observed across the 250 µm section scanned, the µXRF response is limited to a peak in Ca/Ba (see Fig. 6d). [Color figure can be viewed at wileyonlinelibrary.com]

baselines for tephra detection are not very useful. For instance, more than 50 additional peaks would require assessment using the lower Ca threshold level shown in Fig. 2 (dotted line), and over 80% of the cryptotephra layers would remain undetected. Since each investigated peak would contain a significant proportion of ash (especially those caused by remobilisation events), further density separation work using traditional extraction methods would be required to establish their shard profiles and geochemical distinctness. Establishing the eruptive history record for a single compositionally heterogeneous centre such as the Aso caldera, would mean that, at best, only three of the eight eruptions would be identified if µXRF core scanning was used as a first-order method for detection (Table 1). As outlined above, even when the precise stratigraphic interval is known, in many instances no clear geochemical signal could be detected, despite ash concentrations reaching over >20 000 shards per gram. This may be caused by the tight stratigraphic preservation of the glass shards, shown to be constrained to <200 µm in thickness in the varved sediments, and contributing to <20% of the total analysis (Fig. 7). In general, establishing just 10% of the cryptotephrostratigraphy will not be useful for the vast majority of studies aiming to generate comprehensive eruptive records and isochrons for stratigraphic correlation. It is likely that studies that use µXRF core scanning as a first-order technique for cryptotephra identification will be missing other key ash layers, especially those that contain low glass concentrations and thus offer the most valuable and broadest chronostratigraphic tie-points.

We illustrate here that despite these findings, µXRF core scanning can work alongside traditional cryptotephra identification methods to provide new insight into the stratigraphic positioning, and assessment of glass reworking events. In several instances it is possible to use K/Ca and Ti peaks to locate 'cryptic' high-energy events that have remobilised glass from older eruptions. Moreover, for cryptotephra layers that were positively identified, µXRF core scanning allowed their stratigraphic position to be significantly constrained, to less than a millimetre, which allows an improvement in the chronological age modelling (which currently uses the full 1 cm age uncertainty). In the varved sediments of Lake Suigetsu, constraining the position of these layers helps to reduce the age uncertainty. It was also possible to locate the precise varve position using the µXRF core scanning data in conjunction with thin section microscopy, offering significant potential to assign the eruption to a seasonal resolution.

Another advantage of µXRF core scanning is that the compositional signal associated with a tephra is only pronounced over the layer, and the high background shards that occur after the layer often do not affect the signal. This means that µXRF core scanning could be used to detect and verify new, compositionally distinct ash layers in sediments that contain

high background concentrations of glass shards, where density separation methods are not suitable. For instance, we utilised the μXRF data to look for layers in the sediments following the very thick AT tephra that erupted at 30 ka (>50 cm thick) where glass shards from this are reworked through the catchment for over 10 m. Although the visible layers that are in the sediments following the AT tephra are clearly identified, no further cryptotephra layers can be distinguished. Finally, for visible ash layers it may be possible to infer general glass compositions for the layers, if less evolved tephra layers show distinct elemental responses (e.g. key depletions in K, Ti, Fe for Fuji-derived ash), but these characteristics are not comparable to, or a substitute for, single shard geochemical datasets generated using the electron microprobe (see Peti *et al.*, 2020). We are not able to present reliable and universal guidelines for such applications of μXRF core scanning within tephrochronology. While we are able to refine the stratigraphic positioning of ash layers and identify reworking events in the sediments of Lake Suigetsu, these signatures and opportunities will not be universally applicable across other records; for instance, within the marine realm where cryptotephra layers are not as perfectly preserved or sedimentation rates are lower. Moreover, remobilisation signatures will be unique to each archive and are dependent on the setting, sediment composition and volcanic input. Such applications require further detailed investigations using both datasets (μXRF and density separation techniques) in each specific archive.

Factors affecting tephra identification using μXRF core scanning

We find the likelihood of detecting visible and cryptotephra layers using μXRF core scanning depends on three key factors: 1) the host sediment composition and contrast with the composition of the deposited tephra; 2) the palaeoenvironmental sensitivity of the archive (and overprinting of the signals); and 3) the stratigraphic preservation of the glass shards (e.g. concentration, positioning and grain size). The vast majority of tephrostratigraphic studies will use a climatically sensitive archive, and hope to integrate multiple eruption sources through time, meaning conditions to detect cryptotephra layers using μXRF core scanning are likely to be unfavourable at the outset. Perhaps the most critical aspect faced in this example is the geochemical distinction between the tephras and the sediment matrix. The catchment geology surrounding Lake Suigetsu includes granite, dolerite, basalt and chert which forms the host sediments, which are high in Si, Al and Fe and many of the other elements that are abundant in the tephra. Since the compositional baseline is made up of these eroded Si-bearing rocks, the composition of the silicate tephra layers are not radically different and it is impossible to distinguish a signal from the background noise.

Since we used an existing high-resolution μXRF dataset for the Lake Suigetsu sediment cores and do not have data obtained with different analytical settings we can only make some inferences on the scanning parameters. Other analytical changes (e.g. comparing a Cr vs. Mo-tube, increasing the exposure times to >4 s, and the 20 μm step size) could be the focus of future work in different archives and may prove useful, especially if a narrow range of volcanic compositions are expected and can be optimised for. It is unlikely that multiple scanning positions (i.e. offsetting the core centre; see Peti *et al.*, 2020) would improve the success rate in identifying the cryptotephra layers. This is because we do not typically see patchy deposits of ash, and even fine layers remain well constrained and uniform, most clearly observed within the varved structure.

In certain volcanic settings μXRF core scanning may prove to be more useful in delineating tephra positions, especially if less evolved products dominate the record, or are likely to receive tephra from highly potassic sources, which often comprise tephra with high levels of trace element enrichment which exceed host sediment baseline levels (e.g. Zr and Sr). This was demonstrated more successfully in the karstic system at Lake Ohrid (Albania/Macedonia) where peaks in K, Sr and Zr have been used to identify cryptotephra deposits from the Campanian volcanoes (Somma-Vesuvius and Campi Flegrei) (Vogel *et al.*, 2010). Due to the exceptional climatic sensitivity of the Suigetsu sedimentary archive, the lake sediments often show pronounced fine laminations recording both local and regional hydrological and environmental change, which often overprint muted responses caused by tephra. Again, this contrasts with studies using other sedimentary records, like those from the marine environment, where a smaller proportion of the μXRF signal may form peaks, and therefore warrant further investigation for the presence of tephra (e.g. cores analysed from the coast of Monserrat; Cassidy *et al.* 2014).

Conclusions

This study finds that cryptotephra identification by μXRF core scanning is not a suitable standalone technique to establish a comprehensive cryptotephra stratigraphy for a particular sequence. However, it shows that the technique offers a useful tool to accompany more rigorous tephrostratigraphic investigations. For the cryptotephra layers that were identified in the μXRF core scanning, it was possible to refine their stratigraphic position from 1 cm to below a millimetre, thus improving their modelled eruptive age and precision as isochrons. Indeed, in the varved Suigetsu sediments, we show for the first time that cryptotephra shards can be very precisely constrained, spanning just <200 μm in thickness, offering opportunities for ultra-high resolution correlations. Since high concentrations of rhyolitic glass are required to elicit a change in the μXRF elemental signals, core scanning can help identify compositionally distinct tephra layers in sediments that contain high background concentrations of glass shards, and can also help discriminate remobilisation (e.g. reworking) events, which can be notoriously difficult to decipher in cryptotephra stratigraphies. This example using the Suigetsu sediments reveals that μXRF core scanning is useful for the identification of visible tephras, but only recognises 10% of the cryptotephra layers that were identified using density separation techniques. As μXRF data are routinely acquired to provide sedimentological information for key palaeoclimate archives, these data should be investigated for tephra studies but they need to be used in conjunction with standard cryptotephra investigations to generate more complete eruptive records.

Acknowledgements and funding

DM and PGA were funded through a UKRI Future Leaders Fellowship (MR/S035478/1) awarded to PGA. VCS, DM and TN also acknowledge funding from the Japan Society for the Promotion of Science (JSPS; KAKENHI-15H021443). The Fukui-SG06 and SG14 coring campaign was funded by the UK Natural Environmental Research Council (NERC; NE/D000289/1) Investigators Award and the Fukui Prefectural government. The coring was conducted by the team of Seibushisui Co. Ltd Japan, led by Mr Atsumi Kitamura. The glass geochemical datasets referred to in this study can be located in the supplementary materials of the references in

Table 1. Additional datasets can be accessed through the project website (www.suigetsu.org). We thank Dr Leonie Peti and another anonymous reviewer for their constructive comments which helped us to improve the manuscript, and Professor Rewi Newnham for editorial handling.

Conflict of interest statement—The authors have no conflicts of interest to declare.

Supporting information

Additional supporting information can be found in the online version of this article. The glass geochemical data referred to in this study can be located in the supplementary materials of references listed in Table 1. Additional Suigetsu publications and datasets can be accessed through the project website (http://www.suigetsu.org/publications.html).

References

Albert PG, Smith VC, Suzuki T *et al.* 2018. Constraints on the frequency and dispersal of explosive eruptions at Sambe and Daisen volcanoes (South-West Japan Arc) from the distal Lake Suigetsu record (SG06 core). *Earth-Science Reviews* **185**: 1004–1028.

Albert PG, Smith VC, Suzuki T *et al.* 2019. Geochemical characterisation of the Late Quaternary widespread Japanese tephrostratigraphic markers and correlations to the Lake Suigetsu sedimentary archive (SG06 core). *Quaternary Geochronology* **52**: 103–131.

Balascio NL, Francus P, Bradley RS *et al.* 2015. Investigating the use of scanning x-ray fluorescence to locate cryptotephra in minerogenic lacustrine sediment: experimental results, *Micro-XRF Studies of Sediment Cores.* Springer: Dordrecht; 305–324.

Barton RNE, Lane CS, Albert PG *et al.* 2015. The role of cryptotephra in refining the chronology of Late Pleistocene human evolution and cultural change in North Africa. *Quaternary Science Reviews* **118**: 151–169.

Barton RNE, Belhouchet L, Collcutt SN *et al.* 2021. New insights into the late Middle Stone Age occupation of Oued el Akarit, southern Tunisia. *Libyan Studies* **52**: 12–35.

Bergman J, Wastegård S, Hammarlund D *et al.* 2004. Holocene tephra horizons at Klocka Bog, west-central Sweden: aspects of reproducibility in subarctic peat deposits. *Journal of Quaternary Science* **19**(3): 241–249.

Blockley SPE, Pyne-O'Donnell SDF, Lowe JJ *et al.* 2005. A new and less destructive laboratory procedure for the physical separation of distal glass tephra shards from sediments. *Quaternary Science Reviews* **24**(16–17): 1952–1960.

Blockley SP, Bourne AJ, Brauer A *et al.* 2014. Tephrochronology and the extended intimate (integration of ice-core, marine and terrestrial records) event stratigraphy 8–128 ka b2k. *Quaternary Science Reviews* **106**: 88–100.

Brauer A, Casanova J. 2001. Chronology and depositional processes of the laminated sediment record from Lac d'Annecy, French Alps. *Journal of Paleolimnology* **25**(2): 163–177.

Bronk Ramsey CB, Staff RA, Bryant CL *et al.* 2012. A complete terrestrial radiocarbon record for 11.2 to 52.8 kyr BP. *Science* **338**(6105): 370–374.

Buckland HM, Cashman KV, Engwell SL *et al.* 2020. Sources of uncertainty in the Mazama isopachs and the implications for interpreting distal tephra deposits from large magnitude eruptions. *Bulletin of Volcanology* **82**(3): 23.

Cassidy M, Watt SF, Palmer MR *et al.* 2014. Construction of volcanic records from marine sediment cores: A review and case study (Montserrat, West Indies). *Earth-Science Reviews* **138**: 137–155.

Chen XY, Blockley SP, Tarasov PE *et al.* 2016. Clarifying the distal to proximal tephrochronology of the Millennium (B–Tm) eruption, Changbaishan Volcano, northeast China. *Quaternary Geochronology* **33**: 61–75.

Chen XY, McLean D, Blockley SP *et al.* 2019. Developing a Holocene tephrostratigraphy for northern Japan using the sedimentary record from Lake Kushu, Rebun Island. *Quaternary Science Reviews* **215**: 272–292.

Cook E, Portnyagin M, Ponomareva V *et al.* 2018. First identification of cryptotephra from the Kamchatka Peninsula in a Greenland ice core: Implications of a widespread marker deposit that links Greenland to the Pacific northwest. *Quaternary Science Reviews* **181**: 200–206.

Costa A, Folch A, Macedonio G *et al.* 2012. Quantifying volcanic ash dispersal and impact of the Campanian Ignimbrite super-eruption. *Geophysical Research Letters* **39**(10): L10310.

Croudace I, Rothwell G. 2010. Micro-XRF sediment core scanners: Important new tools for the environmental and earth sciences. *SpectroscopyEurope* **22**(3): 6.

Croudace IW, Rindby A, Rothwell RG. 2006. ITRAX: description and evaluation of a new multi-function X-ray core scanner. *Geological Society, London, Special Publications* **267**(1): 51–63.

Damaschke M, Sulpizio R, Zanchetta G *et al.* 2013. Tephrostratigraphic studies on a sediment core from Lake Prespa in the Balkans. *Climate of the Past* **9**(1): 267–287.

Davies SM. 2015. Cryptotephras: the revolution in correlation and precision dating. *Journal of Quaternary Science* **30**(2): 114–130.

Davies SM, Elmquist M, Bergman J *et al.* 2007. Cryptotephra sedimentation processes within two lacustrine sequences from west central Sweden. *The Holocene* **17**(3): 319–330.

Davies SM, Abbott PM, Pearce NJ *et al.* 2012. Integrating the INTIMATE records using tephrochronology: rising to the challenge. *Quaternary Science Reviews* **36**: 11–27.

Davies SJ, Lamb HF, Roberts SJ. 2015. Micro-XRF core scanning in palaeolimnology: recent developments, *Micro-XRF studies of sediment cores.* Springer: Dordrecht; 189–226.

De Vleeschouwer F, van Vliët-Lanoé B, Fagel N *et al.* 2008. Development and application of high-resolution petrography on resin-impregnated Holocene peat columns to detect and analyse tephras, cryptotephras, and other materials. *Quaternary International* **178**(1): 54–67.

Di Roberto A, Smedile A, Del Carlo P *et al.* 2018. Tephra and cryptotephra in a~ 60,000-year-old lacustrine sequence from the Fucino basin: New insights into the major explosive events in Italy. *Bulletin of Volcanology* **80**(3): 20.

Dugmore AJ, Newton AJ. 1992. Thin tephra layers in peat revealed by X-radiography. *Journal of Archaeological Science* **19**(2): 163–170.

Francus P, Lamb H, Nakagawa T *et al.* 2009. The potential of high-resolution X-ray fluorescence core scanning: applications in paleolimnology. *PAGES (Past Global Changes) News* **17**(3): 93–95.

Hall VA, Pilcher JR. 2002. Late-Quaternary Icelandic tephras in Ireland and Great Britain: detection, characterization and usefulness. *The Holocene* **12**(2): 223–230.

Jensen BJ, Pyne-O'Donnell S, Plunkett G *et al.* 2014. Transatlantic distribution of the Alaskan white river ash. *Geology* **42**(10): 875–878.

Jones G, Davies SM, Staff RA *et al.* 2020. Traces of volcanic ash from the Mediterranean, Iceland and North America in a Holocene record from south Wales, UK. *Journal of Quaternary Science* **35**(1-2): 163–174.

Jouannic G, Walter-Simonnet AV, Bossuet G, et al. 2022.Developing and expanding the Late-Glacial and Holocene tephrochronological framework of France: A new contribution from the Chaîne des Puys volcanic field in the Massif Central. *Quaternary International.* https://doi.org/10.1016/j.quaint.2021.12.013

Katsuta N, Takano M, Kawakami SI *et al.* 2007. Advanced micro-XRF method to separate sedimentary rhythms and event layers in sediments: its application to lacustrine sediment from Lake Suigetsu, Japan. *Journal of Paleolimnology* **37**(2): 259–271.

Kearney R, Albert PG, Staff RA *et al.* 2018. Ultra-distal fine ash occurrences of the Icelandic Askja-S Plinian eruption deposits in Southern Carpathian lakes: New age constraints on a continental scale tephrostratigraphic marker. *Quaternary Science Reviews* **188**: 174–182.

Kitagawa H, Van der Plicht H. 1998a. A 40,000-year varve chronology from Lake Suigetsu, Japan: Extension of the C-14 calibration curve. *Radiocarbon* **40**: 505–515.

Kitagawa H, Van der Plicht H. 1998b. Atmospheric Radiocarbon Calibration to 45,000 yr B.P.: Late Glacial Fluctuations and Cosmogenic Isotope Production. *Science* **279**: 1187–1190. Atmospheric Radiocarbon Calibration to 45,000yr B.P.: Late Glacial Fluctuations and Cosmogenic Isotope Production.

Kitagawa H, Fukuzawa T, Nakamura M *et al.* 1995. AMS 14 C dating of varved sediments from Lake Suigetsu, central Japan and atmospheric 14 C change during the late Pleistocene. *Radiocarbon* **37**: 371–378.

Kylander ME, Lind EM, Wastegård S *et al.* 2012. Recommendations for using XRF core scanning as a tool in tephrochronology. *The Holocene* **22**(3): 371–375.

Lane C, Haslam M, Petraglia M *et al.* 2011. Cryptotephra from the 74 ka BP Toba super-eruption in the Billa Surgam caves, southern India. *Quaternary Science Reviews* **30**(15–16): 1819–1824.

Lane CS, Cullen VL, White D *et al.* 2014. Cryptotephra as a dating and correlation tool in archaeology. *Journal of Archaeological Science* **42**: 42–50.

Lane CS, Lowe DJ, Blockley SPE *et al.* 2017. Advancing tephrochronology as a global dating tool: Applications in volcanology, archaeology, and palaeoclimatic research. *Quaternary Geochronology* **40**: 1–7.

Langdon PG, Caseldine CJ, Croudace IW *et al.* 2011. A chironomid-based reconstruction of summer temperatures in NW Iceland since AD 1650. *Quaternary Research* **75**(3): 451–460.

Lim C, Ikehara K, Toyoda K. 2008. Cryptotephra detection using high-resolution trace-element analysis of Holocene marine sediments, southwest Japan. *Geochimica et Cosmochimica Acta* **72**(20): 5022–5036.

Lowe JJ, Ramsey CB, Housley RA *et al.* 2015. The RESET project: constructing a European tephra lattice for refined synchronisation of environmental and archaeological events during the last c. 100 ka. *Quaternary Science Reviews* **118**: 1–17.

MacLeod A, Davies SM. 2016. Caution in cryptotephra correlation: resolving Lateglacial chemical controversies at Sluggan Bog, Northern Ireland. *Journal of Quaternary Science* **31**(4): 406–415.

Marshall M, Schlolaut G, Nakagawa T *et al.* 2012. A novel approach to varve counting using μXRF and X-radiography in combination with thin-section microscopy, applied to the Late Glacial chronology from Lake Suigetsu, Japan. *Quaternary Geochronology* **13**: 70–80.

McCanta MC, Hatfield RG, Thomson BJ *et al.* 2015. Identifying cryptotephra units using correlated rapid, nondestructive methods: VSWIR spectroscopy, X-ray fluorescence, and magnetic susceptibility. *Geochemistry, Geophysics, Geosystems* **16**(12): 4029–4056.

McLean D, Albert PG, Nakagawa T *et al.* 2016. Identification of the Changbaishan 'Millennium'(B-Tm) eruption deposit in the Lake Suigetsu (SG06) sedimentary archive, Japan: synchronisation of hemispheric-wide palaeoclimate archives. *Quaternary Science Reviews* **150**: 301–307.

McLean D, Albert PG, Nakagawa T *et al.* 2018. Integrating the Holocene tephrostratigraphy for East Asia using a high-resolution cryptotephra study from Lake Suigetsu (SG14 core), central Japan. *Quaternary Science Reviews* **183**: 36–58.

McLean D, Albert PG, Suzuki T *et al.* 2020a. Refining the eruptive history of Ulleungdo and Changbaishan volcanoes (East Asia) over the last 86 kyrs using distal sedimentary records. *Journal of Volcanology and Geothermal Research* **389**: 106669.

McLean D, Albert PG, Suzuki T *et al.* 2020b. Constraints on the timing of explosive volcanism at Aso and Aira calderas (Japan) between 50 and 30 ka: New insights from the Lake Suigetsu sedimentary record (SG14 core). *Geochemistry, Geophysics, Geosystems* **21**(8) e2019GC008874.

Moreno A, Giralt S, Valero-Garcés B *et al.* 2007. A 14 kyr record of the tropical Andes: The Lago Chungará sequence (18 S, northern Chilean Altiplano). *Quaternary International* **161**(1): 1–2.

Nakagawa T, Kitagawa H, Yasuda Y *et al.* 2005. Pollen/event stratigraphy of the varved sediment of Lake Suigetsu, central Japan from 15,701 to 10,217 SG vyr BP (Suigetsu varve years before present): description, interpretation, and correlation with other regions. *Quaternary Science Reviews* **24**(14–15): 1691–1701.

Nakagawa T, Gotanda K, Haraguchi T *et al.* 2012. SG06, a fully continuous and varved sediment core from Lake Suigetsu, Japan: stratigraphy and potential for improving the radiocarbon calibration model and understanding of late Quaternary climate changes. *Quaternary Science Reviews* **36**: 164–176.

Panaretos P, Albert PG, Thomas ZA *et al.* 2021. Distal ash fall from the mid-Holocene eruption of Mount Hudson (H2) discovered in the Falkland Islands: New possibilities for Southern Hemisphere archive synchronisation. *Quaternary Science Reviews* **266**: 107074.

Peti L, Gadd PS, Hopkins JL *et al.* 2020. Itrax μ-XRF core scanning for rapid tephrostratigraphic analysis: a case study from the Auckland Volcanic Field maar lakes. *Journal of Quaternary Science* **35**(1–2): 54–65.

Ponomareva V, Portnyagin M, Davies SM. 2015. Tephra without borders: far-reaching clues into past explosive eruptions. *Frontiers in Earth Science* **3**: 83.

Pyne-O'Donnell SD. 2011. The taphonomy of Last Glacial–Interglacial Transition (LGIT) distal volcanic ash in small Scottish lakes. *Boreas* **40**(1): 131–145.

Pyne-O'Donnell SD, Hughes PD, Froese DG *et al.* 2012. High-precision ultra-distal Holocene tephrochronology in North America. *Quaternary Science Reviews* **52**: 6–11.

Reimer PJ, Bard E, Bayliss A *et al.* 2013. IntCal13 and Marine13 radiocarbon age calibration curves 0–50,000 years cal BP. *Radiocarbon* **55**(4): 1869–1887.

Reimer PJ, Austin WE, Bard E *et al.* 2020. The IntCal20 Northern Hemisphere radiocarbon age calibration curve (0–55 cal kBP). *Radiocarbon* **62**(4): 725–757.

Schlolaut G, Marshall MH, Brauer A *et al.* 2012. An automated method for varve interpolation and its application to the Late Glacial chronology from Lake Suigetsu, Japan. *Quaternary Geochronology* **13**: 52–69.

Schlolaut G, Brauer A, Marshall MH *et al.* 2014. Event layers in the Japanese Lake Suigetsu 'SG06'sediment core: description, interpretation and climatic implications. *Quaternary Science Reviews* **83**: 157–170.

Schlolaut G, Staff RA, Brauer A *et al.* 2018. An extended and revised Lake Suigetsu varve chronology from∼ 50 to∼ 10 ka BP based on detailed sediment micro-facies analyses. *Quaternary Science Reviews* **200**: 351–366.

Schindlbeck JC, Kutterolf S, Straub SM *et al.* 2018. One Million Years tephra record at IODP Sites U 1436 and U 1437: Insights into explosive volcanism from the Japan and Izu arcs. *Island Arc* **27**(3): e12244.

Smith VC, Mark DF, Staff RA *et al.* 2011. Toward establishing precise 40Ar/39Ar chronologies for Late Pleistocene palaeoclimate archives: an example from the Lake Suigetsu (Japan) sedimentary record. *Quaternary Science Reviews* **30**(21–22): 2845–2850.

Smith VC, Staff RA, Blockley SP *et al.* 2013. Identification and correlation of visible tephras in the Lake Suigetsu SG06 sedimentary archive, Japan: chronostratigraphic markers for synchronising of east Asian/west Pacific palaeoclimatic records across the last 150 ka. *Quaternary Science Reviews* **67**: 121–137.

Staff RA, Ramsey CB, Bryant CL *et al.* 2011. New 14 C determinations from Lake Suigetsu, Japan: 12,000 to 0 cal BP. *Radiocarbon* **53**(3): 511–528.

Staff RA, Schlolaut G, Ramsey CB *et al.* 2013. Integration of the old and new Lake Suigetsu (Japan) terrestrial radiocarbon calibration data sets. *Radiocarbon* **55**(4): 2049–2058.

Thomson J, Croudace IW, Rothwell RG. 2006. A geochemical application of the ITRAX scanner to a sediment core containing eastern Mediterranean sapropel units. *Geological Society, London, Special Publications* **267**(1): 65–77.

Timms RG, Matthews IP, Lowe JJ *et al.* 2019. Establishing tephrostratigraphic frameworks to aid the study of abrupt climatic and glacial transitions: a case study of the Last Glacial-Interglacial Transition in the British Isles (c. 16-8 ka BP). *Earth-Science Reviews* **192**: 34–64.

Turney CS. 1998. Extraction of rhyolitic component of Vedde microtephra from minerogenic lake sediments. *Journal of Paleolimnology* **19**(2): 199–206.

Turney CS, Lowe JJ, Davies SM *et al.* 2004. Tephrochronology of Last Termination sequences in Europe: a protocol for improved analytical precision and robust correlation procedures (a joint SCOTAV–INTIMATE proposal). *Journal of Quaternary Science* **19**(2): 111–120.

van der Bilt WG, Lane CS, Bakke J. 2017. Ultra-distal Kamchatkan ash on Arctic Svalbard: towards hemispheric cryptotephra correlation. *Quaternary Science Reviews* **164**: 230–235.

Vogel H, Zanchetta G, Sulpizio R *et al.* 2010. A tephrostratigraphic record for the last glacial–interglacial cycle from Lake Ohrid. *Albania and Macedonia. Journal of Quaternary Science25* 320–338.

Wulf S, Ott F, Słowiński M *et al.* 2013. Tracing the Laacher See Tephra in the varved sediment record of the Trzechowskie palaeolake in central Northern Poland. *Quaternary Science Reviews* **76**: 129–139.

Wulf S, Hardiman MJ, Staff RA et al. 2018. The marine isotope stage 1–5 cryptotephra record of Tenaghi Philippon, Greece: towards a detailed tephrostratigraphic framework for the Eastern Mediterranean region. *Quaternary Science Reviews* **186**: 236–262.

Yarincik KM, Murray RW. 2000. Climatically sensitive eolian and hemipelagic deposition in the Cariaco Basin, Venezuela, over the past 578,000 years: Results from Al/Ti and K/Al. *Paleoceanography* **15**: 210e228.

Zawalna-Geer A, Lindsay JM, Davies S *et al.* 2016. Extracting a primary Holocene crytoptephra record from Pupuke maar sediments, Auckland, New Zealand. *Journal of Quaternary Science* **31**: 442–457.